



Deposited via The University of Sheffield.

White Rose Research Online URL for this paper:

<https://eprints.whiterose.ac.uk/id/eprint/218634/>

Version: Published Version

Article:

Biswal, S., Korsós, M.B., Georgoulis, M.K. et al. (2024) Case studies on pre-eruptive X-class flares using R-value in the lower solar atmosphere. *The Astrophysical Journal*, 974. 259. ISSN: 0004-637X

<https://doi.org/10.3847/1538-4357/ad6c33>

Reuse

This article is distributed under the terms of the Creative Commons Attribution (CC BY) licence. This licence allows you to distribute, remix, tweak, and build upon the work, even commercially, as long as you credit the authors for the original work. More information and the full terms of the licence here:







<https://creativecommons.org/licenses/>

Takedown

If you consider content in White Rose Research Online to be in breach of UK law, please notify us by emailing eprints@whiterose.ac.uk including the URL of the record and the reason for the withdrawal request.



Case Studies on Pre-eruptive X-class Flares using R -value in the Lower Solar Atmosphere

Shreeyesh Biswal^{1,2} , Marianna B. Korsós^{3,4,5} , Manolis K. Georgoulis^{6,7} , Alexander Nindos² , Spiros Patsourakos² , and Robertus Erdélyi^{1,4,5} 

¹ Solar Physics & Space Plasma Research Center (SP2RC), School of Mathematics and Statistics, University of Sheffield, Hounsfield Road, Sheffield, S3 7RH, UK

² Department of Physics—Section Astrogeophysics, University of Ioannina, Ioannina—45110, Greece

³ University of Sheffield, Department of Automatic Control and Systems Engineering, Amy Johnson Building, Portabello Street, Sheffield, S1 3JD, UK

⁴ Department of Astronomy, Eötvös Loránd University, Pázmány Péter sétány 1/A, Budapest H-1117, Hungary

⁵ Gyula Bay Zoltan Solar Observatory (GSO), Hungarian Solar Physics Foundation (HSPF), Petőfi tér 3., Gyula H-5700, Hungary

⁶ Johns Hopkins University Applied Physics Laboratory Laurel, MD 20375, USA

⁷ Research Center for Astronomy and Applied Mathematics of the Academy of Athens, 11527 Athens, Greece

Received 2024 April 18; revised 2024 July 22; accepted 2024 July 26; published 2024 October 16

Abstract

The R -value is a measure of the strength of photospheric magnetic polarity inversion lines in active regions (ARs). This work investigates the possibility of a relation between R -value variations and the occurrence of X-class flares in ARs, not in the solar photosphere, as usual, but above it in regions closer to where flares occur. The modus operandi is to extrapolate the Solar Dynamic Observatory's Helioseismic and Magnetic Imager magnetogram data up to a height of 3.24 Mm above the photosphere and then compute the R -value based on the extrapolated magnetic field. Recent studies have shown that certain flare-predictive parameters such as the horizontal gradient of the vertical magnetic field and magnetic helicity may improve flare prediction lead times significantly if studied at a specific height range above the photosphere, called the optimal height range (OHR). Here, we define the OHR as a collection of heights where a sudden but sustained increase in R -value is found. For the eight case studies discussed in this paper, our results indicate that it is possible for OHRs to exist in the low solar atmosphere (between 0.36 and 3.24 Mm), where R -value spikes occur 48–68 hr before the first X-class flare of an emerging AR. The temporal evolution of R -value before the first X-class flare for an emerging AR is also found to be distinct from that of nonflaring ARs. For X-class flares associated with nonemerging ARs, an OHR could not be found.

Unified Astronomy Thesaurus concepts: [Solar flares \(1496\)](#); [Solar chromosphere \(1479\)](#); [Solar corona \(1483\)](#); [Solar photosphere \(1518\)](#); [Solar active region magnetic fields \(1975\)](#); [Space weather \(2037\)](#)

1. Introduction

A solar flare is an intense burst of electromagnetic radiation from the Sun. It is caused due to magnetic reconnection in the solar atmosphere (Kopp & Pneuman 1976). Early models that addressed the relation between solar flares and magnetic reconnection were two-dimensional (2D) in nature, with one of the most popular being the CSHKP “standard flare” model (Carmichael 1964; Sturrock 1966; Hirayama 1974; Kopp & Pneuman 1976). Thanks to advancements in space research and technology, solar energetic phenomena, including the standard flare model, are now studied in three dimensions (3D) via magnetohydrodynamic (MHD) models (Janvier 2017; Korsós et al. 2018; Pontin & Priest 2022). Solar flares are often associated with eruptive phenomena called coronal mass ejections (CMEs). A CME is an ejection of a sizable coronal magnetic structure, thought to be a helical magnetic flux rope, into the heliosphere (Low 1994; Dere et al. 1999). When this flux rope (also known as a magnetic cloud in the interplanetary space) is directed toward Earth, it has the potential to interact with the terrestrial geomagnetic field. This interaction may induce a geomagnetic storm and cause damage to our technosphere from space all the way to the Earth's surface for major disturbances.

Solar flares and CMEs are two distinct manifestations of a common underlying mechanism of magnetic energy release (Gosling 1990; Low 1994; Harrison 1995; Gopalswamy 2016). Solar flare X-ray intensity fluxes are indeed well correlated to their corresponding CME energies (Youssef 2012). Other studies show the relation between flares and CMEs as the synchronization of flare emissions (HXR and temporal derivative of SXR) and CME acceleration (Zhang et al. 2004; Temmer et al. 2010). Since it is known that stronger flares, especially X-class events (X-ray intensity flux greater than 10^{-4} Wm⁻²), have a high probability of CME association (Yashiro et al. 2005), predicting X-class flares is a problem of particular importance in space-weather research.

The key physical process leading to the manifestation of active regions (ARs) is the emergence of toroidal magnetic flux tubes in the photosphere due to buoyancy in the convection zone (Parker 1955; Parker 1979). MHD models have successfully simulated and accounted for the inception of flux in the photosphere and its subsequent transport to the corona in 2D (Shibata et al. 1989; Kaisig et al. 1990; Shibata et al. 1990) and 3D (Fan 2001; Archontis et al. 2004). Physical processes such as the evolution of an unstable flux rope (Aulanier et al. 2010; Aulanier et al. 2012; Kusano et al. 2012) and the evolution of the current layer and magnetic reconnection in 3D have also been studied extensively (Janvier et al. 2013; Kliem et al. 2013; Janvier 2017). One way to predict solar flares is to track the changes occurring in the magnetic flux patterns of flare-producing ARs and assess how they differ from ARs that do not produce

flares. Toriumi & Wang (2019) give an overview of processes and features associated with the formation of flare-producing ARs. Significant processes linked to the production of flare-producing ARs include the formation of δ -sunspots (Künzel 1959; Sammis et al. 2000; Tian et al. 2002) and the appearance of high-gradient magnetic polarity inversion lines (PILs) in the photosphere (Falconer et al. 2002; Falconer et al. 2003; Schrijver 2007). Sammis et al. (2000) further showed that more complex sunspots, especially the ones identified to be δ , $\beta\delta$, and $\beta\gamma\delta$ produce stronger flares and that flare strength (in terms of peak X-ray irradiance) is positively correlated with sunspot area.

Detailed tracking of PIL evolution is also useful to predict flares. PILs are interfaces between flux patches of opposite magnetic polarity, where the vertical magnetic field component B_z “neutralizes” (i.e., becomes zero) along them. The presence of high-gradient PILs, where the vertical magnetic field component enhances dramatically just off the PIL, is a characteristic eruptive flare source pattern and such PILs are often an outcome of shearing of the photospheric magnetic field and convergence of opposite-polarity flux patches (Georgoulis et al. 2019). Morphological parameters such as G_M and WG_M , that take the horizontal gradient of the vertical magnetic flux into account, have also been previously introduced (Korsós et al. 2014, 2015). For the calculation of G_M , two areas having the maximum positive and the maximum negative magnetic polarities are identified and the difference between their fluxes is divided by the distance between their area weighted centroids. WG_M is a more generalized form of G_M where the calculation includes not two but several regions of opposite polarities. With regards to the PILs, there exist several other morphological parameters, such as unsigned flux, PIL gradients (Falconer et al. 2002; Falconer et al. 2003), R -value (Schrijver 2007), effective connected magnetic field strength (Georgoulis & Rust 2007), and length (total and maximum) of PILs (Mason & Hoeksema 2010) that could be used to address solar flare prediction probability quantitatively. Schrijver (2007) found that when the peak R -value computed in the photosphere reaches about 2×10^{21} Mx, then the probability of occurrence of a major flare in 24 hr is close to unity. PILs can also be studied from the perspective of electric current density directly, instead of studying proxies of magnetic nonpotentiality, but this requires the full magnetic field vector. In fact, strong PILs are the only photospheric structures that support non-neutralized electric currents, such as in a nonzero volume current in coronal flux tubes (Georgoulis et al. 2012). From a study on the temporal evolution of non-neutralized currents, Kontogiannis et al. (2017) established a correspondence between them and key physical processes such as the appearance of PILs and flux rope formation. Having provided a brief outline of parameters (or predictors) that mathematically incorporate several key features directly linked to solar flare productivity, it is noteworthy to mention that a total of 209 such “predictors” have been identified by the European Union’s Flare Likelihood and Region Eruption predicting (FLARECAST) project (Georgoulis et al. 2021). The FLARECAST project (2015–18)⁸ conclusively showed that, due to stochasticity in flare occurrence, flare prediction is an inherently probabilistic problem (Campi et al. 2019).

Recent developments in solar flare prediction have suggested that the prediction of flare onset can be improved by several

hours, if key predictors are studied above the photosphere in the lower solar atmosphere (LSA). For example, from a study of 13 flare-producing ARs of Solar Cycle 24 (SC24), Korsós et al. 2020 showed that it may be possible to improve prediction lead time by 2–8 hr by tracking the temporal evolution of the WG_M morphological parameter at a height range of 1000–1800 km in the LSA instead of carrying out the same exercise in the photosphere. This LSA height range of 1000–1800 km serves, then, as an optimal height range (OHR). Motivated by these promising results, the objective of this paper is to systematically explore the concept of OHR with the R -value parameter. An application of this concept is core to the Solar Activity Magnetic Monitor Network (SAMNet⁹) that aims to achieve, in practice by their proposed ground-based sentinel network, an improved flare forecasting by determining the OHR (Erdélyi et al. 2022).

This paper is mainly centered around the R -value parameter, which in basic terms is a quantification of the unsigned flux near high-gradient PILs. The outline of this paper is as follows. Section 2 focuses on the analysis procedure and it contains a detailed description of the algorithm used for the computation of R -value. The essence of the algorithm, which is to detect high-gradient PILs in a given magnetic field map, is described within the context of the second step, presented in Section 2. Section 3 contains information on the AR data set and the criteria used for the selection of ARs. The results and discussion are presented in Section 4, followed by the summary and conclusions in Section 5. Additional pertinent information is described in the Appendix.

2. Analysis Method

The overall analysis procedure can be described in three main steps:

First, for each AR, a potential-field (PF) extrapolation of the radial component of the magnetic field is performed using as input the Solar Dynamic Observatory’s (SDO)/Helioseismic and Magnetic Imager (HMI) 2D Spaceweather HMI Active Region Patch (SHARP) vector magnetogram corresponding to the AR (Pesnell et al. 2012; Scherrer et al. 2012). If the area corresponding to a given SHARP includes more than one AR, it is suitably cropped to isolate the AR under focus. This is the case for NOAA ARs 11520 and 12017. The extrapolation is performed up to a height of 3.24 Mm in the LSA using 10 discrete planes, each spaced 0.36 Mm apart from its neighboring planes. The cadence of choice is 1 hr. We use a linear force free field (LFFF) extrapolation technique that relies on the fast Fourier transform approach. Naturally, a PF extrapolation is achieved by setting the force-free parameter α to zero (Alissandrakis 1981; Gary 1989). Although PF extrapolation has its limitations, it is precise enough for a first-hand estimate, mathematically simpler, and quicker to operate compared to more sophisticated extrapolations (e.g., Korsós et al. 2024). By using the PF extrapolation, we are looking at the photospheric morphology over long timescales, without the intention of modeling dynamical features in the lower solar atmosphere (for reference, see Wiegmann & Sakurai 2012; for applications see Korsós et al. 2020 and Korsós et al. 2022). The output of this step is a 3D data-grid of the vertical magnetic field component B_z —we do not use the horizontal potential field. A sample visualization of the 3D data-grid is shown in Figure 1.

⁸ <http://flarecast.eu/>

⁹ <http://hsfpf.eu/samnet.html>

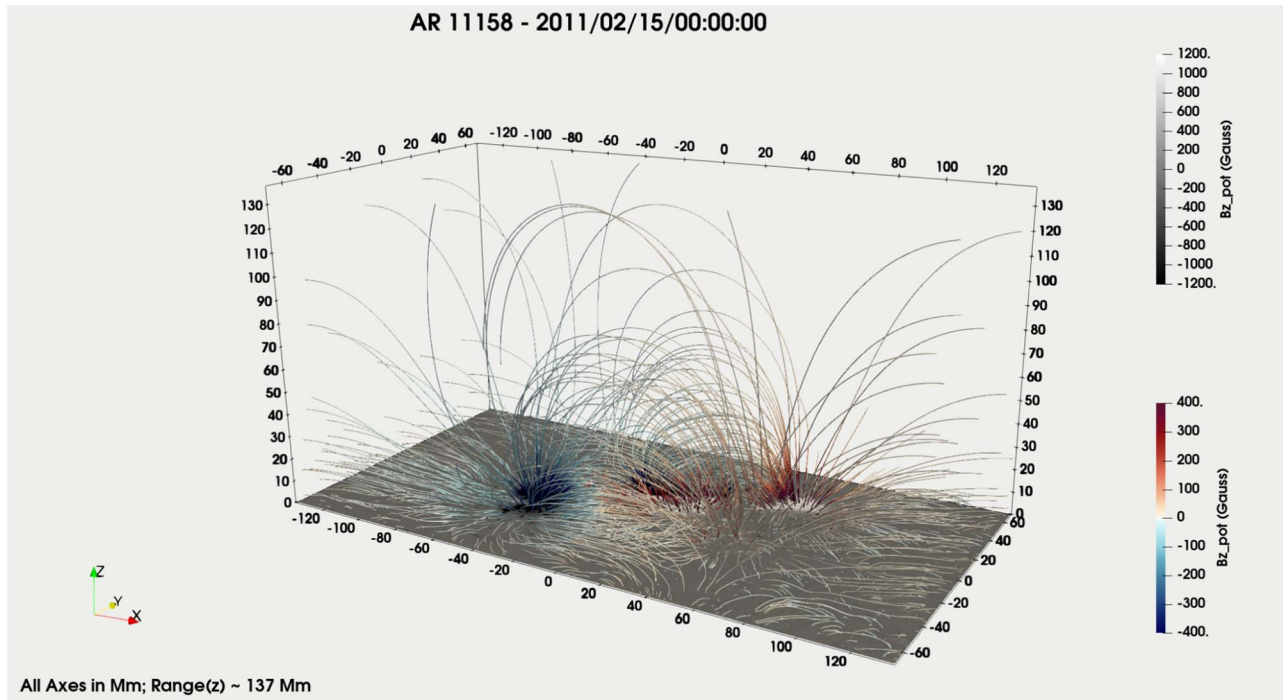


Figure 1. A 3D visualization of the PF-extrapolated magnetic field for AR 11158 at 00:00 UTC, 2011 February 15, created using Paraview (<https://www.paraview.org/>); the colorbar in top right-hand corner denotes the B_z values at the photosphere (map at the bottom of the grid, also reproduced in Figure 2(a)); the colorbar in the bottom right-hand corner denotes extrapolated B_z values. The colorbars have been saturated to ± 1200 G on the photosphere and to ± 400 G above the photosphere. The data has been taken from an ISEE open-source database (<https://hinode.isee.nagoya-u.ac.jp/>), courtesy of Kusano et al. (2020).

Second, starting with the 3D data-grid, the unsigned flux ϕ near PILs and R -value are computed in the 0–3.24 Mm height range at 1 hr cadence for the time windows specified in Table 2 (Section 3). The codes used to compute the unsigned magnetic flux near PILs and R -value are adapted from the FLARECAST Bitbucket Project Repository.¹⁰ The algorithm used for computing the R -value is an adaptation of the one described in Schrijver (2007). The difference is that we use the radial field component from vector magnetograms, while Schrijver (2007) used the line-of-sight (LoS) component. Estimating the R -value relies on two input parameters: magnetic field threshold B_{th} and separation distance D_{sep} , which control the identification of high-gradient PILs. The threshold B_{th} is used to compute bitmaps corresponding to positive and negative flux. In the positive polarity bitmap, the elements are assigned the value “1” where $B_z > +B_{\text{th}}$ and “0” otherwise. Similarly, in the negative-polarity bitmap, the elements are assigned the value “1” where $B_z < -B_{\text{th}}$ and “0” otherwise. These bitmaps are then dilated and their product yields a map M where high-field regions can be identified from nonzero values. The map “ M ”, indicating high-polarity regions, is then convolved with an area-normalized Gaussian G (characterized by a FWHM = D_{sep}), resulting in a weight map W that assigns more weight to regions closer to high-gradient PILs as opposed to regions that are further apart (see Equation (1)).

$$W = M(B_{\text{th}}) * G(D_{\text{sep}}). \quad (1)$$

This weight map is then multiplied with the original magnetogram data (or magnetic field map) B_{map} . Examples of the resulting output maps are shown in Figure 2. The sum of absolute values of all elements multiplied with an area element A gives the R -value (see Equation (2)). A ($\sim 0''.5$) is

approximately 1.3141×10^{15} cm² in CGS units.

$$R_{\text{val}} = A \sum_{ij} |B_{\text{map}}|_{ij} \cdot W_{ij}. \quad (2)$$

Third, following the R -value calculation in the photosphere and above, the data are visualized with the help of stack plots varying as a function of time (see the GitHub project repository¹¹ for all stack plots and codes). Since the exact dependence of R -value on B_{th} and D_{sep} is not known, the R -value is computed for different combinations of B_{th} and D_{sep} (see Table 1). Schrijver (2007) argued that, statistically, a threshold $B_{\text{th}} = 150$ G could be used. Since the extrapolated fields are weaker than photospheric fields, and since our choice of B_{th} does not vary with height, using a lower threshold for B_{th} is helpful to identify high-gradient PILs at higher altitudes. The noise level associated with the photospheric data is ~ 10 G (Liu et al. 2012). Therefore, it is not helpful to reduce B_{th} below 50 G. On D_{sep} , Schrijver (2007) found that two thirds of the values of the distribution for D (i.e., the minimum distance between a PIL and the brightest point in the EUV images) were less than 15 Mm. Hence, Schrijver (2007) took $D_{\text{sep}} = 15$ Mm for the computation of R -value on the photosphere.

3. AR Dataset

We selected eight ARs that hosted 11 X-class solar flares within a certain time interval of interest in each case (see Table 2). We chose these ARs and their corresponding temporal windows for two main reasons. First, in order to ensure that the magnetic field data is reliable for extrapolation. Since magnetic field observations have severe projection effects beyond 60° from the solar central meridian (Bobra et al. 2014), all these ARs

¹⁰ <https://dev.flarecast.eu/stash/projects/FE/repos>

¹¹ https://github.com/shreeyesh-biswal/Rvalue_3D

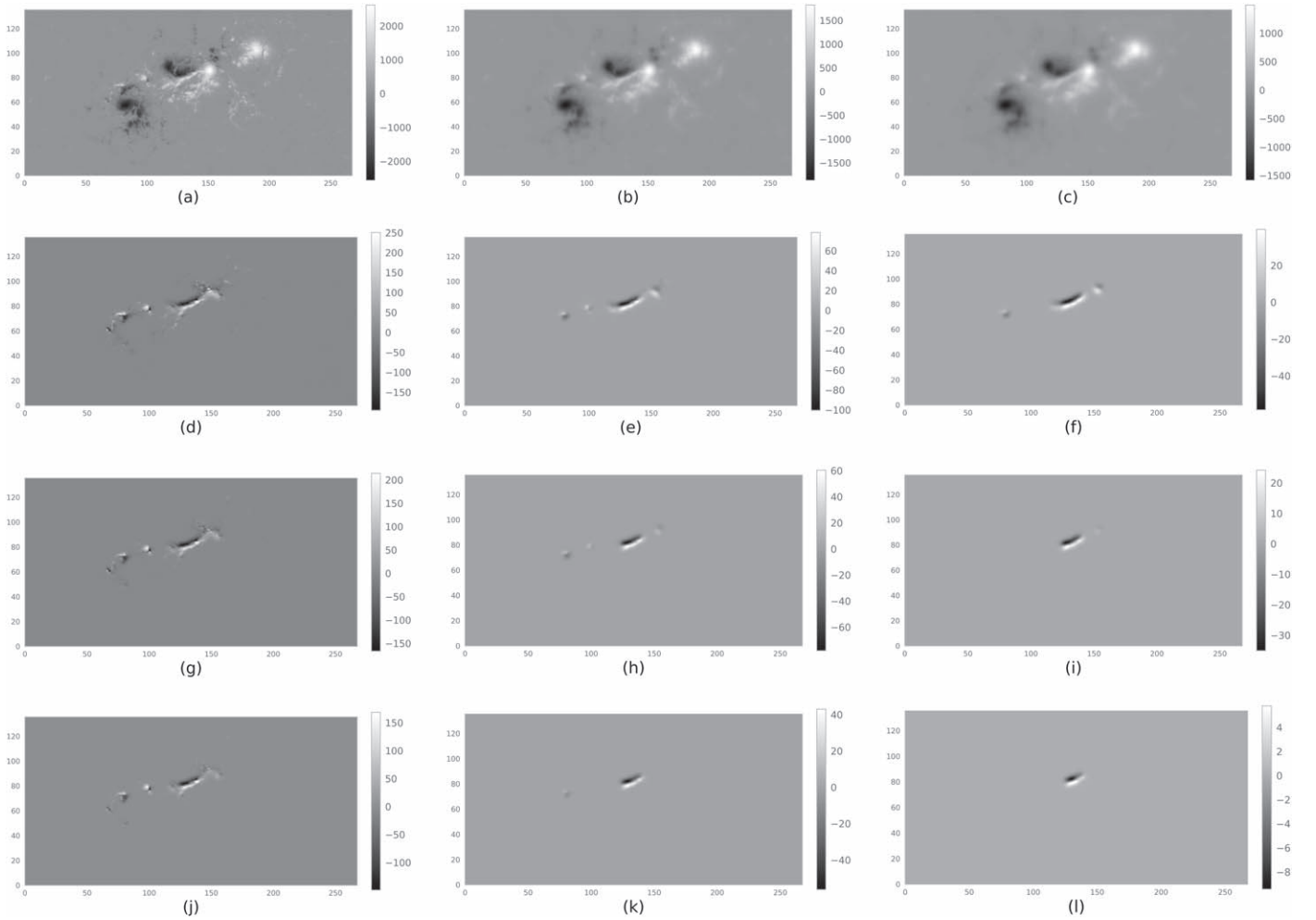


Figure 2. Plots corresponding to AR 11158 on 2011 February 15 00:00 UTC; (a)–(c): B_z maps at the photosphere, 1.08 Mm and 1.80 Mm, respectively; (d)–(f): $R_{(50,15)}$ maps corresponding to magnetic field maps (a)–(c), respectively; (g)–(i): $R_{(100,15)}$ maps corresponding to magnetic field maps (a)–(c), respectively; (j)–(l): $R_{(150,15)}$ maps corresponding to magnetic field maps (a)–(c) respectively. The colorbars in magnetograms (a)–(c) denote B_z (G), while in all other maps they represent B_z (G) after the application of filtering. It is important to note how at higher altitudes (maps (f), (i), and (l)), due to weakening of the field, the high-gradient regions tend to become more localized.

Table 1

Model Specifications and Notations for the Calculation of the R -value

Experimental Models for R -value			
No.	B_{th}	D_{sep}	Model Notation
01	150 G	15 Mm	$R_{(150,15)}$
02	150 G	10 Mm	$R_{(150,10)}$
03	100 G	15 Mm	$R_{(100,15)}$
04	50 G	15 Mm	$R_{(50,15)}$
05	50 G	10 Mm	$R_{(50,10)}$

Note. We alternate between values of 10 and 15 Mm for D_{sep} and we use three different values for B_{th} , namely 50, 100, and 150 Gn.

were located within 60° EW throughout their corresponding time windows. Second, at any time within these time intervals of interest, each of the listed ARs hosted a δ -sunspot, which is a feature indicating the presence of high-gradient PILs. All ARs have a minimum interval of 48 hr between the observational start time and the corresponding flare onset. The objective is to examine whether knowledge of an imminent X-class flare is possible at least 24 hr in advance. Furthermore, we require that the SDO/HMI SHARP magnetogram data are continuously

available for at least 120 hr. The HMI data product used is the Lambert cylindrical equal-area projection of the photospheric vector magnetic field, identifiable by the following extension: hmi.sharp_cea_720s.

4. Results and Discussion

After a set of numerical sensitivity tests on several ARs, it was found that changing D_{sep} from 15 to 10 Mm did not impact R -value as much as changing B_{th} from 150 to 100 or 50 G. We took into account the statistical findings of Schrijver (2007) while selecting the numerical values for B_{th} and D_{sep} prior to the sensitivity tests. For the sake of brevity, one representative example is presented in Appendix A. For more examples, please visit the GitHub project repository. For simplicity, we keep D_{sep} fixed at 15 Mm, considering only R -value results obtained from the following pairs of thresholds $R_{(B_{th}, D_{sep})}$: $R_{(150,15)}$, $R_{(100,15)}$ and $R_{(50,15)}$. The similarity of patterns in (i) $R_{(50,15)}$ and $R_{(50,10)}$ and (ii) $R_{(150,15)}$ and $R_{(150,10)}$ can be seen in Figure 11 (Appendix A). The preflare R -value trends are classified into two categories based on whether the unsigned flux increases or decreases near PILs, before the occurrence of first X-class flare for each AR. However, there was also the

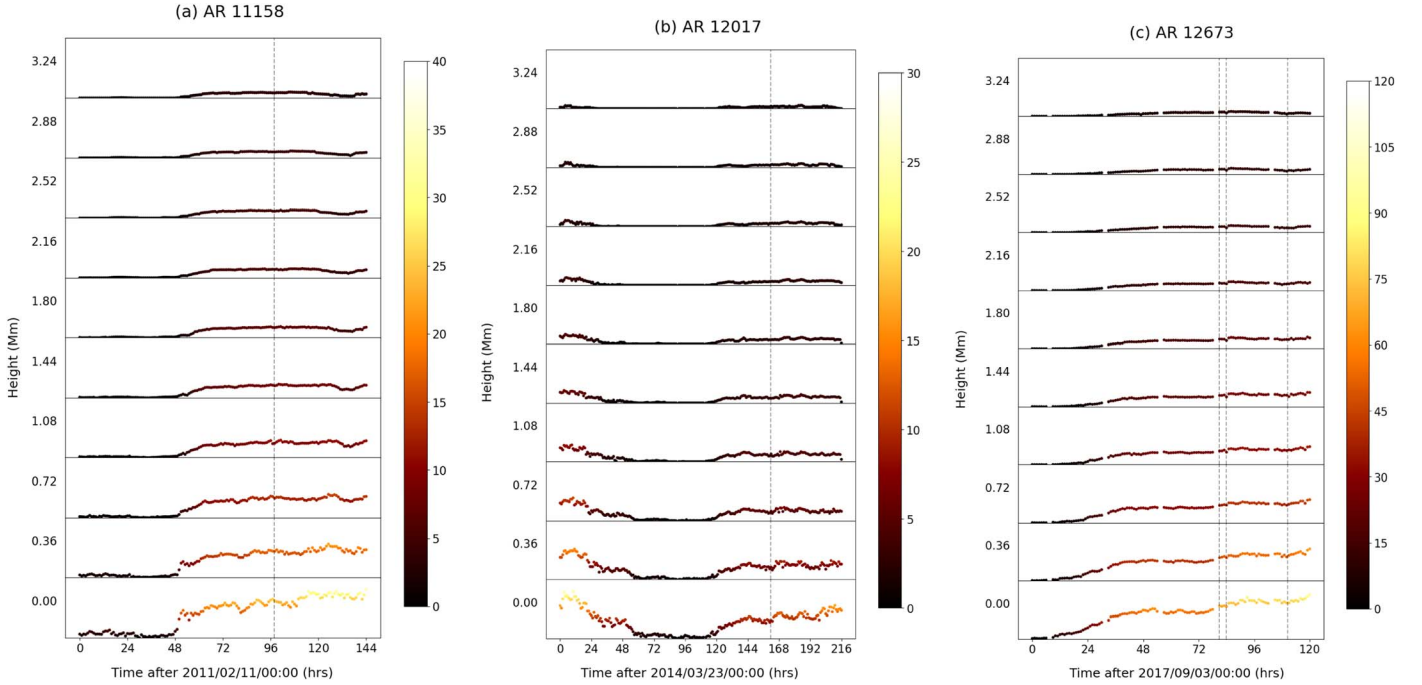
Sample plots for Unsigned Flux near PILs (in 10^{20} Mx)

Figure 3. Multiple-height stack plots for unsigned flux near PILs for (a) AR 11158, (b) AR 12017, and (c) AR 12673; colorbar indicates the unsigned flux (in 10^{20} Mx). Flux emergence is observed prior to the occurrence of X-class flare in each case (marked by vertical dashed lines in each plot).

Table 2

The Details of the Studied ARs, GOES Flare Classes, Observation Intervals (Between T_{start} and T_{end}), Flare Onset Time ($T_{\text{flare onset}}$), Time Difference Between Flare Onset and Start of the Observing Interval (in Hours), and SHARP Linear Dimensions (in Mm^2)

Observed Data								
No.	AR	Class	T_{start}	T_{end}	$T_{\text{flare onset}}$	$T_{\text{flare onset}} - T_{\text{start}}$ (hr)	SHARP Size (Mm^2)	
01	11158	X2.2	2011/02/11 00:00	2011/02/17 00:00	2011/02/15 01:44	97.73	267.48 \times 135.36	
02	11166	X1.5	2011/03/05 00:00	2011/03/10 00:00	2011/03/09 23:13	119.22	263.52 \times 137.16	
03	11283	X2.1	2011/09/01 00:00	2011/09/09 00:00	2011/09/06 22:12	142.2	351.00 \times 182.16	
		X1.8	2011/09/01 00:00	2011/09/09 00:00	2011/09/07 22:32	166.53	351.00 \times 182.16	
04	11520	X1.4	2012/07/08 00:00	2012/07/15 00:00	2012/07/12 15:37	111.62	234.00 \times 180.00	
05	12017	X1.0	2014/03/23 00:00	2014/04/01 00:00	2014/03/29 17:35	161.58	230.76 \times 87.48	
06	12158	X1.6	2014/09/07 00:00	2014/09/14 00:00	2014/09/10 17:21	89.35	202.68 \times 191.16	
07	12297	X2.1	2015/03/09 00:00	2015/03/15 00:00	2015/03/11 16:11	64.18	358.20 \times 215.64	
08	12673	X2.2	2017/09/03 00:00	2017/09/08 00:00	2017/09/06 08:57	80.95	247.32 \times 160.92	
		X9.3	2017/09/03 00:00	2017/09/08 00:00	2017/09/06 11:53	83.88	247.32 \times 160.92	
		X1.3	2017/09/03 00:00	2017/09/08 00:00	2017/09/07 14:20	110.33	247.32 \times 160.92	

case of AR 11283 that fell into neither of these categories, which has been discussed in detail in Appendix B. In Section 4.3, the variation of R -value for nonflaring cases has been presented to help the reader understand how it differs from the cases immediately before an X-class flare (refer to Sections 4.1 and 4.2). Assuming that preflare conditions prior to the occurrence of X-class flares in ARs are radically different from quiescent ARs, we have also explored the R -value in height and time for a few intermediate cases. In Appendix C, 4 ARs have been discussed where the R -value is studied prior to the occurrence of the first M-class flare in each case. A similar study, but for an AR with a δ sunspot hosting only C-class flares, is also presented in Appendix C. A detailed discussion on the lead time is presented in Section 4.4. Finally, Section 4.5 presents a preliminary idea of how we envision the R -value to

be relevant toward the development of a novel flare-prediction method.

4.1. ARs Associated with a Prior Increase in the Unsigned Flux near PILs

Before the occurrence of the first X-class flare for ARs 11158, 11166, 12017, and 12673, a significant increase is seen in both the unsigned flux and R -value (see Figure 11(a) in Appendix A for AR 11166 and Figure 3 for other ARs). Qualitatively, therefore, there is some degree of correlation between the temporal variation of the R -value on the photosphere and unsigned flux near PILs for these ARs (compare Figure 3(a) with Figures 4(a), (b) and (c), especially at the panel corresponding to the photosphere). It is already known that flux emergence near PILs is linked to X-class flaring

R-value plots for AR 11158

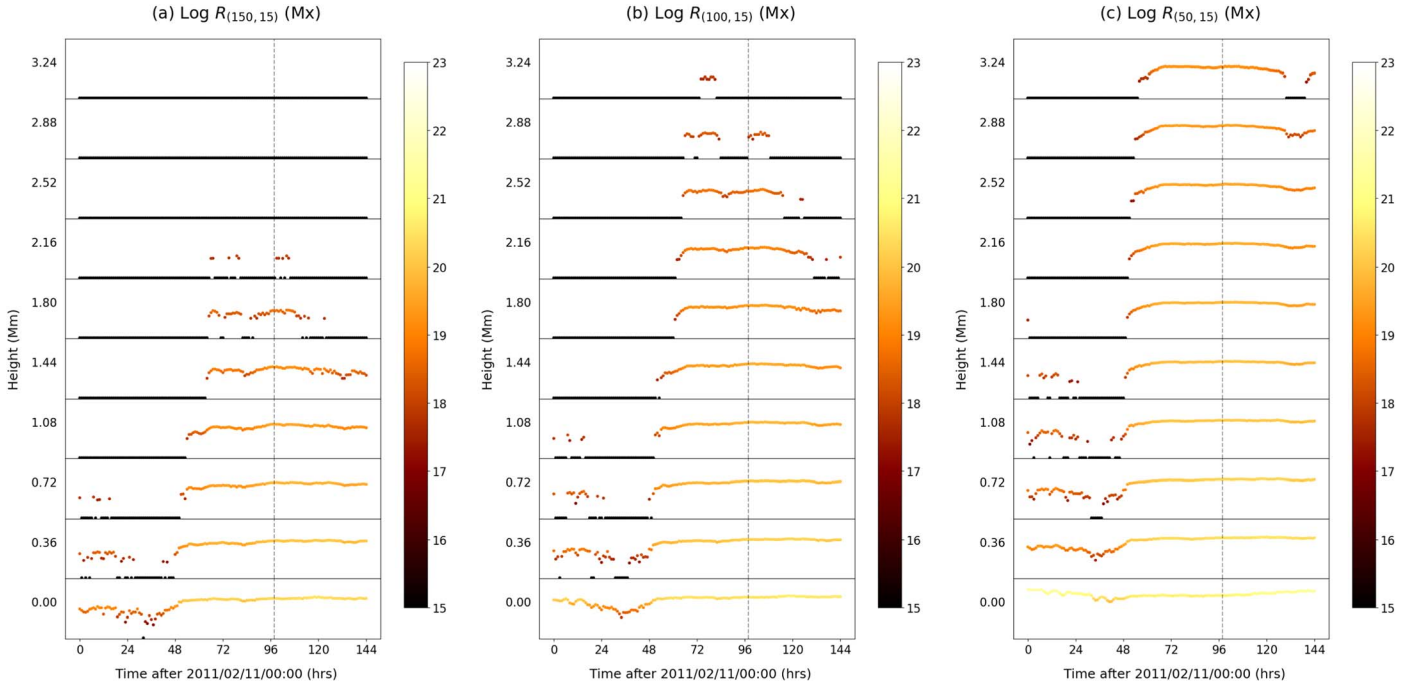


Figure 4. Multiple-height stack plots for (a) $R_{(150,15)}$, (b) $R_{(100,15)}$, and (c) $R_{(50,15)}$; vertical dashed line indicates the time of occurrence of the X2.2 flare; colorbar indicates the logarithm of R -value (in Mx); any black lines or points indicate null output. The OHRs in this case are as follows: (a) 0.36–1.44 Mm, (b) 0.36–2.52 Mm, and (c) 1.08–3.24 Mm. For $R_{(50,15)}$, we do not consider 0.72 Mm within the OHR because the black line is continuous for less than 6 hr.

Table 3Table Comparing Changes in $R_{(150,15)}$ and ϕ for ARs 11158, 11166, 12017, and 12673 at T_{fe} and T_{fo} in the Photosphere

Unsigned Flux ϕ Near PILs and $R_{(150,15)}$ (Both in 10^{20} Mx) at T_{fe} and T_{fo}						
AR	T_{fe}	$\phi (T_{fe})$	$R_{(150,15)} (0 \text{ Mm})$	T_{fo}	$\phi (T_{fo})$	$R_{(150,15)} (0 \text{ Mm})$
11158	2011/02/13 01:00	5.63	0.24	2011/02/15 01:00	25.54	2.31
11166	2011/03/06 16:00	5.93	0.18	2011/03/09 23:00	30.76	2.40
12017	2014/03/28 00:00	2.94	0.05	2014/03/29 17:00	8.30	0.76
12673	2017/09/03 18:00	12.70	0.87	2017/09/06 06:00	61.17	7.35

activity (Toriumi 2022). However, since we find the jump in R -value at about the same time, we hypothesize that the jump in R -value could be linked to flaring activity, although a statistical study may still be needed to verify this. The exact procedure of identifying a jump in R -value is discussed in the next paragraph. For the purpose of simplicity, we introduce two parameters; (i) T_{fe} denoting the time of flux emergence near PILs on the photosphere and (ii) T_{fo} denoting the latest time-stamp in our data set just before flare onset. For ARs 11158, 12017, and 12673, T_{fe} indicates the time when a sharp increase in the unsigned flux was observed. For AR 11166, T_{fe} indicates the time when the flux shows a consistently increasing trend following a period of decrease. Table 3 lists the values of the unsigned flux around PILs and the photospheric R -values at T_{fe} and T_{fo} . Using these values, we can make a quantitative estimate of the increase of these parameters. For example, in case of AR 11158, the flux at T_{fo} was about five times the value at T_{fe} , while the photospheric R -value at T_{fo} was about 10 times the value at T_{fe} . This suggests that for AR 11158, high-gradient PILs contribute to a higher share in the total flux around PILs immediately before a flare compared to the time when flux

emergence is observed. Similar trends are seen for ARs 11166, 12017, and 12673 (refer to Table 3).

AR 11158 hosted the first X-class flare of SC24 at 01:44 UTC on 2011 February 15. The sunspot group that was $\beta\gamma$ -type on 2011 February 11, transformed into a $\beta\gamma\delta$ -type sunspot on February 16, within a day of the eruption of the X2.2 flare. It can be seen from Figure 3(a) that flux levels on February 16 were higher compared to the preflare levels (Feb 11–12). Let us consider the $R_{(150,15)}$ trends in height for AR 11158 (Figure 4(a)). It may be seen that at some time around T_{fe} at 0.36 Mm altitude, the black line (denoting null output from the code; owing to weak fields not breaching B_{th}) disappears and $R_{(150,15)}$ suddenly jumps. This suggests that strong magnetic flux begins to emerge at 0.36 Mm at around T_{fe} . This is also indicative of a high-gradient PIL setup in the extrapolated magnetic field map at 0.36 Mm. At higher altitudes (up to 1.44 Mm), the jump in $R_{(150,15)}$ is observed at later moments in time compared to the temporal variation seen at 0.36 Mm. For $R_{(150,15)}$, we consider the height range of 0.36–1.44 Mm as the OHR. So, here, the OHR is to be understood as a collection of heights where a clear and sustained jump in R -value is observed. Please note here that a jump is identified in retrospect

Table 4

R-value Increase Times within the OHRs for AR 11158; T_{rv} for any Given Model, Indicates the First Time-stamp where Nonzero *R*-value Output was Computed Following a Continuous Period of Null Values

<i>R</i> -value Increase Times T_{rv} for Different <i>R</i> -value Models (AR 11158)			
Height (in Mm)	$T_{rv}[R_{(150,15)}]$	$T_{rv}[R_{(100,15)}]$	$T_{rv}[R_{(50,15)}]$
0.00	---	---	---
0.36	2011/02/13 00:00	2011/02/12 14:00	---
0.72	2011/02/13 03:00	2011/02/13 00:00	---
1.08	2011/02/13 06:00	2011/02/13 03:00	2011/02/12 23:00
1.44	2011/02/13 16:00	2011/02/13 07:00	2011/02/13 01:00
1.80	---	2011/02/13 13:00	2011/02/13 02:00
2.16	---	2011/02/13 14:00	2011/02/13 03:00
2.52	---	2011/02/13 17:00	2011/02/13 04:00
2.88	---	---	2011/02/13 06:00
3.24	---	---	2011/02/13 08:00

when after a period of null *R*-value output, the *R*-value begins to show some finite value continuously for minimum duration of 6 hr. The choice of time interval (i.e., 6 hr in this case) is somewhat subjective and has been deliberately introduced to distinguish between data and noise, the noise being cases where the *R*-value fluctuates between zero and finite values at timescales shorter than 6 hr. Additional constraints to define the jump may be imposed as more examples (i.e., flare-producing ARs) are studied in future. Within the context of OHR, we define T_{rv} , which denotes the time of *R*-value increase, i.e., the time when the *R*-value begins to show some finite value after a period of null output. In essence, post the T_{rv} , the *R*-value must not descend back to null values (e.g., depicted by black lines in Figure 4) and it must have been preceded by black lines continuously for a minimum of 6 hr. Table 4 lists the times of *R*-value increase at different heights for AR 11158.

Computing *R*-value with a B_{th} of 150 G, at higher altitudes often leads to continuous flat black lines, indicating null *R*-values (see Figure 4(a)). This is because the extrapolated B_z is weaker compared to the photospheric B_z and the B_{th} of 150 G is too high to detect high-polarity regions. The results obtained for the magnetic structure model constructed with $R_{(100,15)}$ for AR 11158 are consistent with what has been observed from the $R_{(150,15)}$ model. The *R*-value increase times are close to T_{fe} just like the $R_{(150,15)}$ model but the OHR is extended further up to 2.52 Mm (refer to Table 4). For the $R_{(100,15)}$ model at 0.36 Mm, the black lines are indicative of the time window when $R_{(100,15)}$ is really low in the photosphere (see panels corresponding to 0 and 0.36 Mm in Figure 4(b)). However, for heights between 0.72 and 1.44 Mm, the time window corresponding to the black lines largely coincides with the time when the unsigned flux is really low before it begins to increase (compare Figures 3(a) and 4(b)). In the case of $R_{(50,15)}$, the OHR is between 1.08 and 3.24 Mm. It is important to note here that the time of increase in $R_{(50,15)}$ is more consistent in height compared to that of $R_{(150,15)}$ and $R_{(100,15)}$ (compare Figure 4(c) with Figures 4(a) and (b)).

Overall, a progressive increase in the sunspot group complexity was observed either throughout or for a significant part of the observation time window for the “emergent” ARs 11158, 11166, 12017, and 12673. For example, for AR 11166, the complexity of the sunspot group changed from β -type on 2011 March 4, to $\beta\gamma$ -type on March 6 and subsequently to $\beta\gamma\delta$ -type on 2011 March 8. We find that as the sunspot becomes more complex and as we approach the X-class flare in time, the

R-value seems to sustain nonzero values at higher altitudes. For example, on March 5, the highest altitude where $R_{(150,15)}$ is fairly continuously nonzero is 0.36 Mm but on March 9, $R_{(150,15)}$ we find nonzero values at 1.44 Mm (see Figure 11(b)). This shows that there may be a link between the height-wise variation of the *R*-value as a function of time and the temporal evolution of the sunspot group complexity.

For AR 12017, at first the flux is high (see Figure 3(b) around March 23–24) and the flux drops to near-zero values and begins to increase significantly again. The *R*-value also shows a similar trend. Upon inspecting the *R*-value in the photosphere, we find a “V” shape trend. This pattern becomes more noticeable at higher altitudes as we can see the plotted black lines corresponding to null outputs in *R*-value, such as 0.36 Mm for $R_{(150,15)}$ or 1.44 Mm for $R_{(50,15)}$ (see Figure 5).

Unlike ARs 11158, 11166, and 12017, an isolated X-class flare was not observed for AR 12673, rather, a series of four X-class flare events were observed (three of which occurred within the $\pm 60^\circ$ from the disk center). It is also important to note that in the 72 hr preceding the first of these X-class flares, 12 M-class flares were reported in AR 12673. For AR 12673, the increase in unsigned flux was more gradual compared to ARs 11158, 11166, and 12017, and T_{fe} coincides with the time when magnetic bipoles emerge around the central PIL (Liu et al. 2019). The first flare with a magnitude X2.2 occurs at a time when a steady increase in the flux is seen (see Figure 3). An OHR can be determined from all models; 0.72–2.88 Mm for $R_{(150,15)}$, 1.08–3.24 Mm for $R_{(100,15)}$, and 1.44–3.24 Mm for $R_{(50,15)}$ (see Figure 6). To sum up, all these OHRs have one common feature, by being between 1 and 3 Mm. In general, at higher altitudes, the computation of *R*-value loses scientific relevance because of weak field strengths.

4.2. ARs Associated with a Prior Decrease in the Unsigned Flux Near PILs

Sometimes, X-class flares may occur during a period of gradual decrease in the unsigned flux near PILs, as in the cases of ARs 11520, 12158, and 12297 (see Figure 7). While for ARs 11520 and 12158, decreases in $R_{(50,15)}$, $R_{(100,15)}$ and $R_{(150,15)}$ were observed with the passage of time (see Figure 8 as a sample) across different heights, for AR 12297, $R_{(50,15)}$, $R_{(100,15)}$, and $R_{(150,15)}$ remained nearly constant in time across different heights. In summary, the *R*-value trends from these cases did not yield anything conclusive and an OHR could not be defined or determined. However, a common feature for all

R-value plots for AR 12017

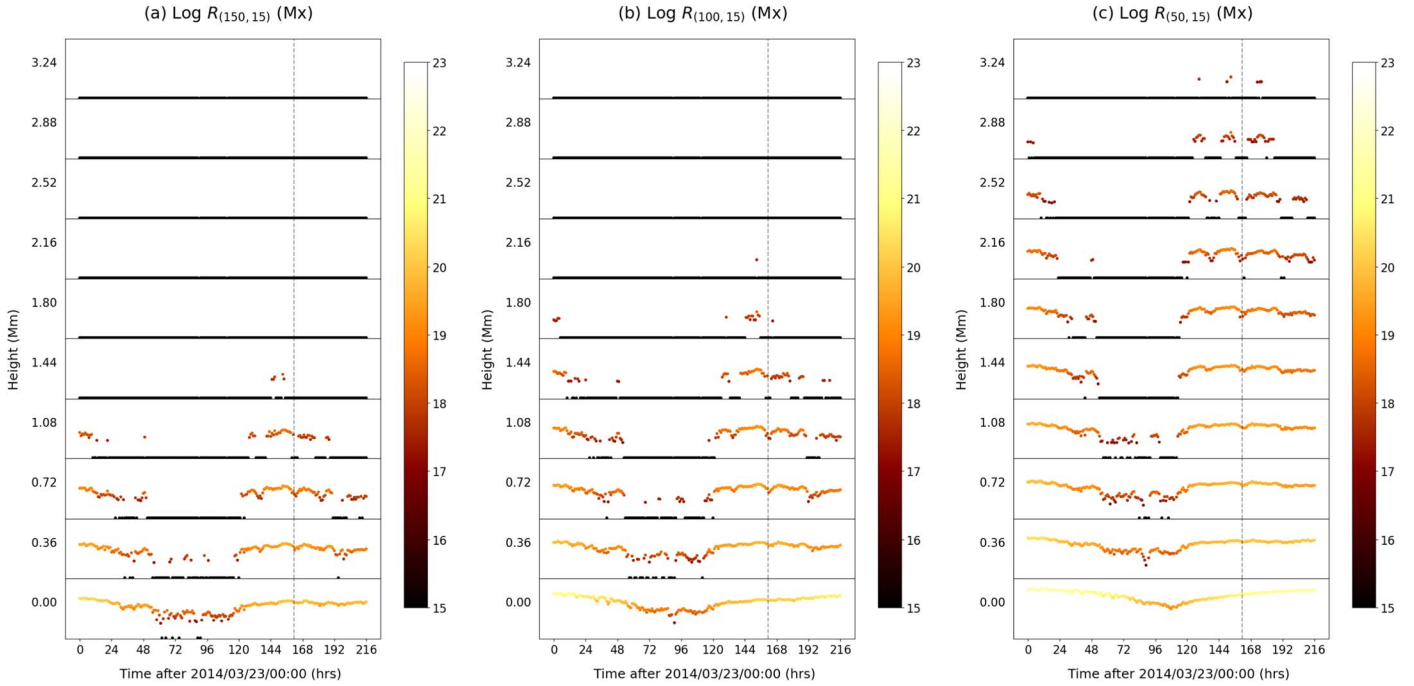


Figure 5. Multiple-height stack plots for (a) $R_{(150,15)}$, (b) $R_{(100,15)}$, and (c) $R_{(50,15)}$; vertical dashed line indicates the time of occurrence of the X1.0 flare; colorbar indicates the logarithm of R -value (in Mx); any black lines or points indicate null output. The OHRs in this case are as follows: (a) 0.36–1.08 Mm, (b) 0.72–1.44 Mm, and (c) 1.08–2.16 Mm.

R-value plots for AR 12673

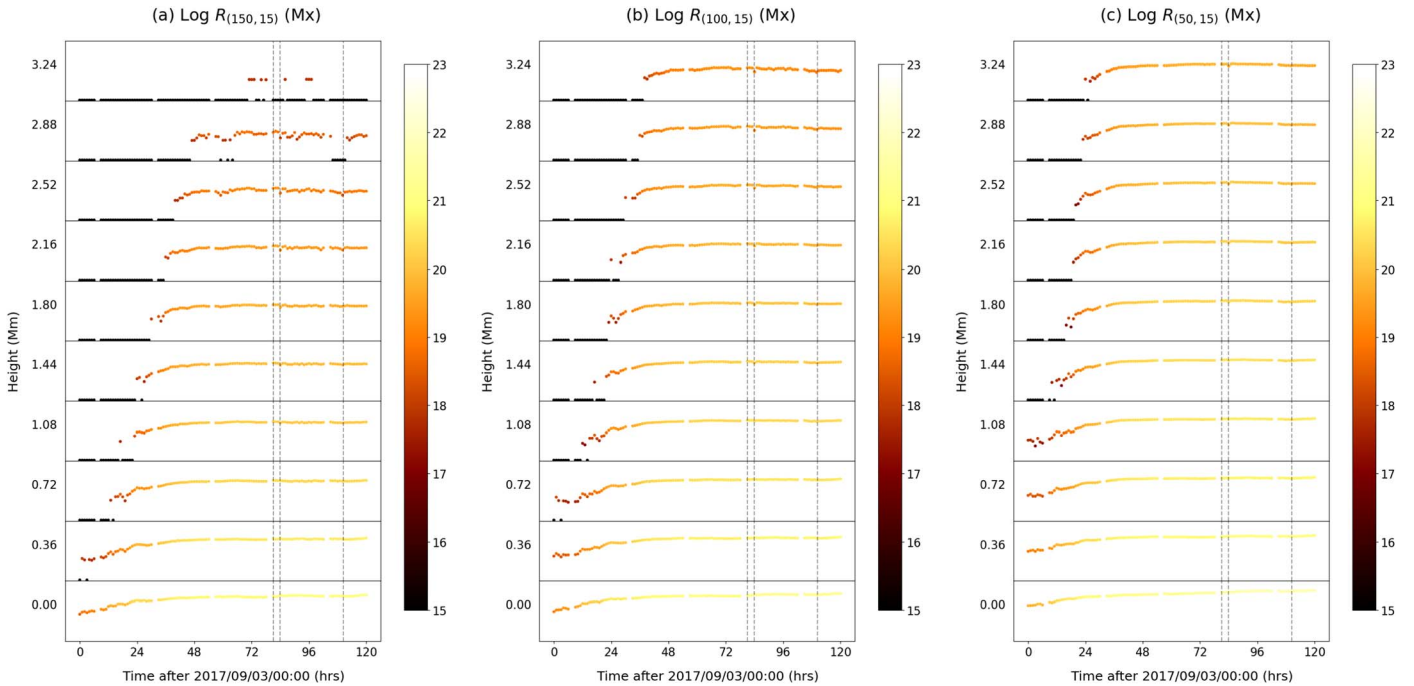


Figure 6. Multiple-height stack plots for (a) $R_{(150,15)}$, (b) $R_{(100,15)}$, and (c) $R_{(50,15)}$; vertical dashed lines indicate time of occurrence of X-class flares; colorbar indicates the logarithm of R -value (in Mx); any black lines or points indicate null output. The OHRs in this case are as follows: (a) 0.72–2.88 Mm, (b) 1.08–3.24 Mm, (c) 1.44–3.24 Mm.

these ARs is that they were not emergent ARs and were almost always associated with a complex sunspot group throughout the observation time. For example, AR 12158 initially hosted a β δ -type sunspot that transformed into a β γ δ -type before

eventually decreasing its complexity to γ δ -type sunspot toward the end of the observation time. For AR 11520, the black line at 1.80 Mm for the $R_{(150,15)}$ model (about 60 hr before the X1.4 flare) is almost consistent in time after 09:00 UTC on 2012 July

Plots for Unsigned Flux near PILs

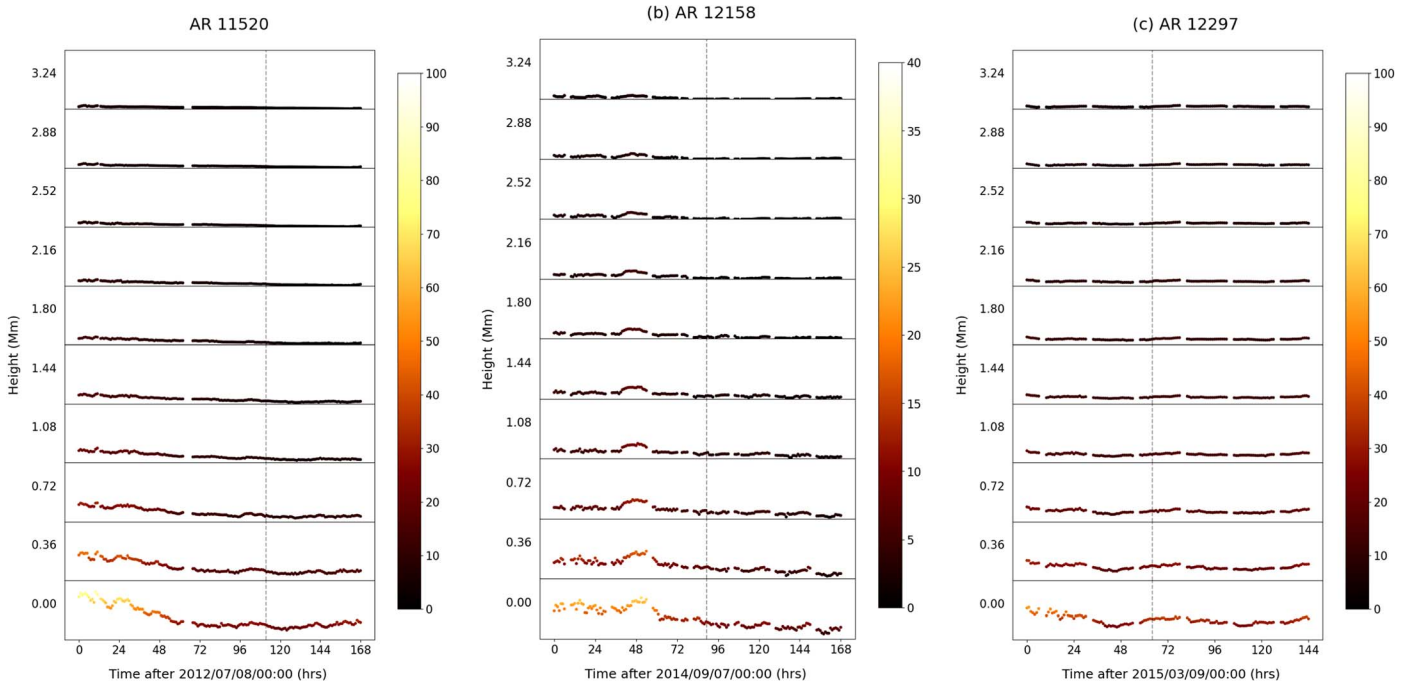


Figure 7. Multiple-height stack plots for unsigned flux near PILs for (a) AR 11520, (b) AR 12158, and (c) AR 12297; colorbar indicates the unsigned flux (in 10^{20} Mx); vertical dashed line in each plot indicates time of occurrence of the X-class flare.

R-value plots for AR 11520

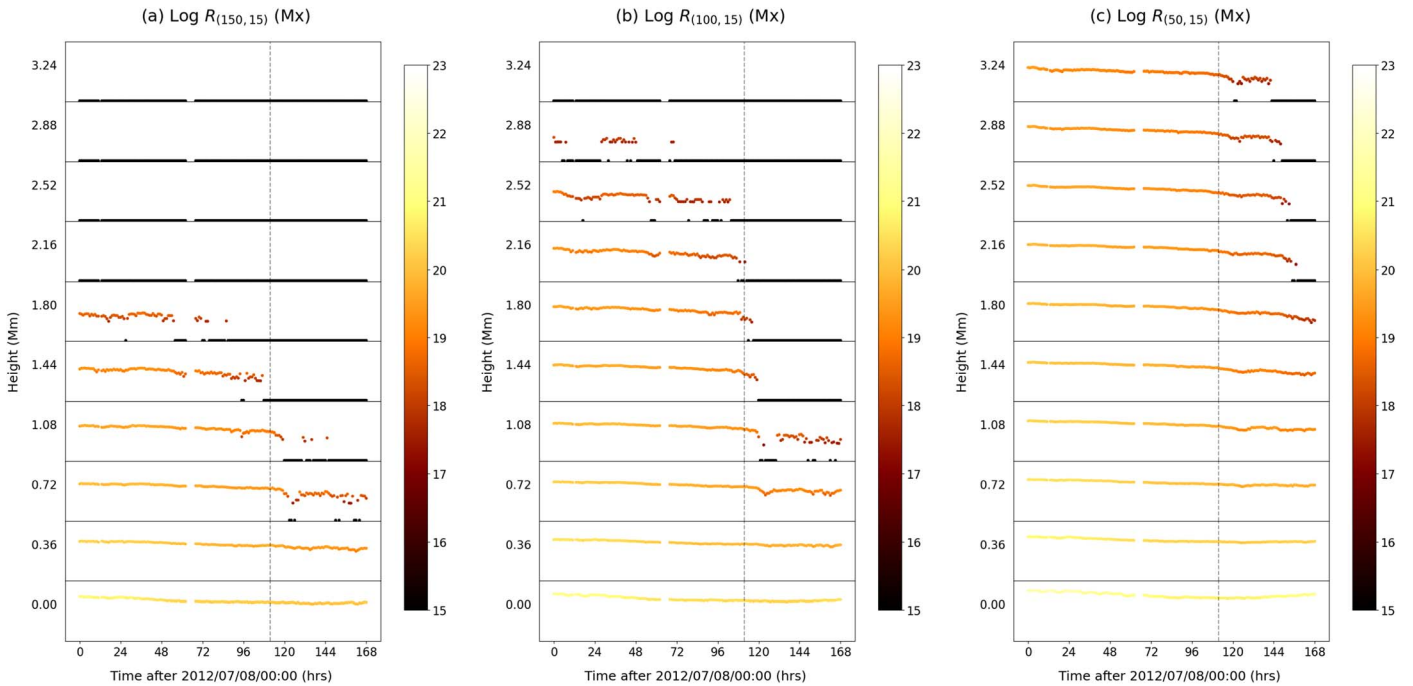


Figure 8. Multiple-height stack plots for (a) $R_{(150,15)}$, (b) $R_{(100,15)}$, and (c) $R_{(50,15)}$; vertical dashed line indicates time of occurrence of the X1.4 flare; colorbar indicates the logarithm of R-value (in Mx); any black lines or points indicate null output.

10 (see Figure 8). It may be an intuitive idea to propose that the R-value disappearance may be linked to X-class flares. However, at this stage, we refrain from proposing such a hypothesis because of the lack of a sufficient number of examples; therefore, retaining the idea as a “conjecture,”

subject to a more extensive study in the future. It is known that eruptive solar flares at times could be driven by magnetic flux cancellation (Zhang et al. 2001; Burtseva & Petrie 2013) and it might be possible that the X-class flares related to ARs 11520, 12158, and 12297 were related to magnetic flux cancellation.

Sample R-value plots for non-flaring cases

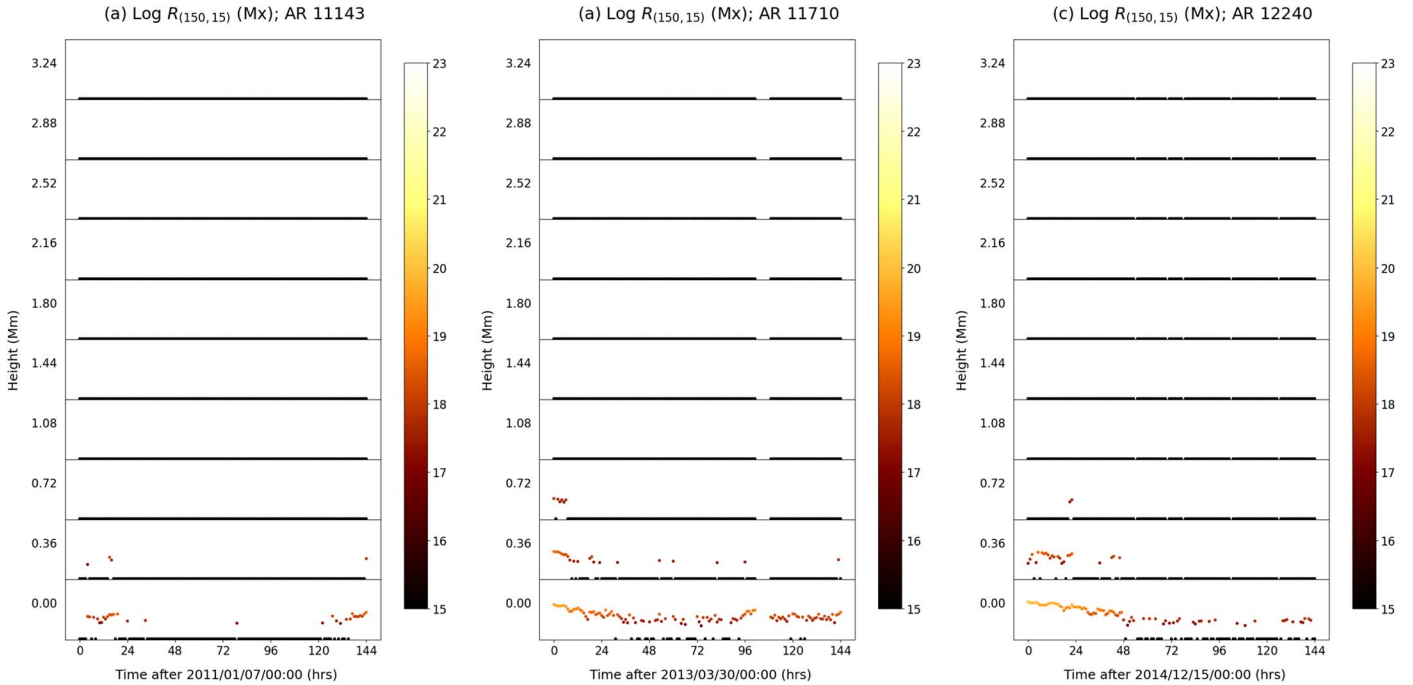


Figure 9. Multiple-height $R_{(150,15)}$ stack plots for nonflaring cases (a) AR 11143, (b) AR 11710, and (c) AR 12240; colorbar indicates the logarithm of R -value (in Mx); any black lines or points indicate null output.

4.3. R-value in Height and Time for Nonflaring ARs

The vertical variation of $R_{(150,15)}$ may be used as a discriminant flaring and nonflaring ARs. We consider an AR to be nonflaring if it does not host any flares stronger than C1.0. We studied three nonflaring cases: AR 11143 (2014 January 7–13), AR 11710 (2013 March 30–April 5), and AR 12240 (2014 December 15–21). All these ARs hosted a β sunspot during the time window of study. PF extrapolation followed by computation of R -value in 3D showed that $R_{(150,15)}$ does not consistently sustain nonzero values at 0.36 Mm for AR 11143 or barely does so for ARs 11710 and 12240. This is clearly distinct from what we observed for X-class flares and even M-class flares (see Appendix C). For the M-class or X-class flare cases, we find that the maximum height where $R_{(150,15)}$ sustains nonzero values can be as low as 0.72 Mm and as high as 3.24 Mm. Some sample results for the nonflaring ARs are shown in Figure 9. Although we have restricted the discussion to the variation of $R_{(150,15)}$ as a discriminant at the photosphere (or low altitudes), it is important to note that if we reduce B_{th} , the R -value may still sustain nonzero values at altitudes greater than 0.72 Mm (see GitHub project repository for examples). $R_{(50,15)}$ and $R_{(100,15)}$ may still serve as discriminants between flaring and nonflaring ARs but more examples are needed to be studied for further confirmation.

4.4. Physical Significance of Results

We were able to identify OHRs for ARs linked to flux emergence, i.e., ARs 11158, 11166, 12017, and 12673, and the special case of AR 11283 (see Appendix B). For a given AR and its OHR, a T_{rv} (i.e., the time of R -value increase) was determined for all heights included in the OHR. The difference between T_{rv} and the latest time-stamp preceding the flare T_{pf} gives T_{diff} , which is an estimate of the lead time. Rather than

using the exact time of flare occurrence, T_{pf} was used so as to keep T_{diff} an integer for convenience. The height-wise variation of the lead time is listed in Tables 11, 12, and 13, corresponding to $R_{(150,15)}$, $R_{(100,15)}$, and $R_{(50,15)}$, respectively (see Appendix D). To visualize the data in conjunction with flare strength, we have presented Figure 10.

A general inference from the height-wise lead time data is that as we approach the flare in time, the lead time decreases. However, the nature (linear/nonlinear) or rate of decrease is different for different ARs. In certain cases, this decrease may follow a linear trend. For example, linear regression calculations for the $R_{(150,15)}$ lead time versus height plot for AR 12673 showed a R^2 value of 0.97 (see Figure 10 (left-hand panel)). The data also suggests that flare strength may not be well correlated with lead time. For example, the lead time-height curves for AR 11158 and AR 11166 intersect between 0.72 and 1.08 Mm, suggesting that there may not be any particular correlation between flare strength and lead time. While at 0.72 Mm the weaker flare (X1.5; AR 11166) is associated with a higher lead time, at 1.08 Mm the stronger flare (X2.2; AR 11158) is associated with a shorter lead time. This aspect needs to be studied further with a larger statistical sample for further conclusions. For $R_{(50,15)}$, the OHR is most likely to occur at heights greater than 1.08 Mm (upto 3.24 Mm) but for $R_{(150,15)}$, it may be expected between 0.36 and 1.44 Mm (see Tables 11 and 13). The most frequently occurring heights in the OHRs for $R_{(50,15)}$, $R_{(100,15)}$, and $R_{(150,15)}$ are 1.08, 1.44, and 2.16 Mm, respectively. This indicates that if we reduce B_{th} , an OHR may be expected at higher altitudes. Furthermore, the height range discussed above, where the jump of the R -value is more pronounced, aligns with the findings of Korsós et al. (2024). The authors have indicated that utilizing a variety of precursor parameters is important in the LSA (up to 2 Mm) to enhance the accuracy of eruption predictions. In addition, certain

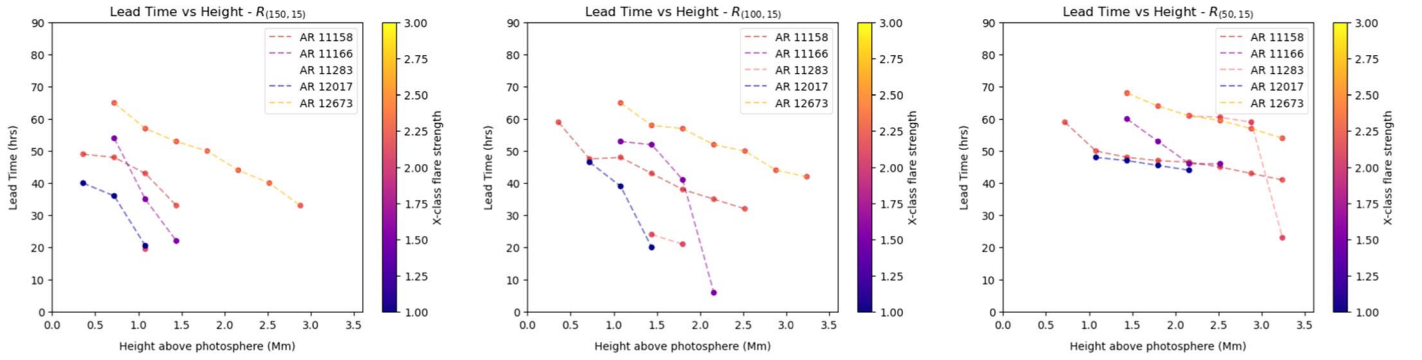


Figure 10. Plots between lead time (i.e., T_{diff}) and height for five different ARs with an OHR for $R_{(150,15)}$ (left-hand panel), $R_{(100,15)}$ (middle panel) and $R_{(50,15)}$ (right-hand panel). The colorbar in each plot denotes flare strength in terms of peak soft X-ray flux (in 10^{-4} Wm^{-2}). For exact numerical values of T_{diff} , refer to Tables 11, 12, and 13 in Appendix D.

Table 5

A List of Optimal Times and Response Times for each OHR for X-Class Flare Cases

No. (1)	AR (2)	Flare (3)	T_{pf} (4)	T_{diff}^* [$R_{(150,15)}$] (5)	T_{diff}^* [$R_{(100,15)}$] (6)	T_{diff}^* [$R_{(50,15)}$] (7)	T_{opt} (8)	$T_{\text{res}} = T_{\text{opt}} - C_{\text{int}}$ (9)
01	11158	X2.2	2011/02/15 01:00	49 hr	59 hr	50 hr	59 hr	35 hr
02	11166	X1.5	2011/03/09 23:00	54 hr	53 hr	60 hr	60 hr	36 hr
03	11283	X2.1	2011/09/06 22:00	20 hr	24 hr	61 hr	61 hr	37 hr
04	11520	X1.4	2012/07/12 15:00	---	---	---	---	---
05	12017	X1.0	2014/03/29 17:00	40 hr	47 hr	48 hr	48 hr	24 hr
06	12158	X1.6	2014/09/10 17:00	---	---	---	---	---
07	12297	X2.1	2015/03/11 16:00	---	---	---	---	---
08	12673	X2.2	2017/09/06 08:00	65 hr	65 hr	68 hr	68 hr	44 hr

Note. Column (4) lists the latest time-stamp preceding the flare T_{pf} . Columns (5)–(7) list the maximum lead time across all heights T_{diff}^* for $R_{(150,15)}$, $R_{(100,15)}$, and $R_{(50,15)}$, respectively. The maximum T_{diff}^* across multiple R -value models is T_{opt} and is listed in column (8). Column (9) lists the response time T_{res} after subtracting the confidence interval C_{int} from T_{opt} . For exact information on T_{diff} and T_{diff}^* , refer to Tables 11, 12, and 13. Optimal times are indicated in bold.

proxies have been observed to reveal their own preflare evolution phase earlier within the LSA (Korsós et al. 2018, 2020, 2022).

4.5. Proposed Application of Results to Solar Flare Prediction

In this section we describe how the R -value may be employed to predict the first X-class flare for an emerging AR in a real-time scenario. We emphasize that the ideas proposed here are simply based on the case studies encountered so far and the exact method to be used in case of prediction must be based on the results from a rigorous statistical study, which is beyond the scope of the current paper. To estimate how much time in advance a prediction can be issued in a best-case scenario, we introduce a new term T_{diff}^* that denotes the maximum lead time across all heights in an OHR for an AR. Although T_{diff}^* gives the maximum time available to issue a prediction for a specific R -value model, it is important to note that this time difference has been obtained only in hindsight. In a real-time prediction scenario, a jump in R -value from zero to nonzero values temporarily may not necessarily imply a sudden change in solar activity because it is possible that it might very well be noise. So, in the event of a real-time prediction scenario, we further impose the condition that the R -value must sustain nonzero values for at least 24 hr after increase so that a prediction warning may be issued with some confidence. This period of 24 hr can be thought of as a “confidence interval” (denoted by C_{int}), which is once again somewhat indicative/conjecture-oriented. Our choice of C_{int} has been decided on the basis of AR examples we have encountered so far and C_{int} may

need modification as more examples are studied in future. Based on inputs from the three R -value models, the maximum value of T_{diff}^* across different R -value models may be considered as the optimal time T_{opt} . The T_{opt} for each case (or AR) is indicated in bold (refer to Table 5). The C_{int} was then subtracted from T_{opt} to obtain an estimate of the response time T_{res} (refer to Table 5). The idea behind defining T_{res} is to quantify the time available to respond to a flare warning after an alert has been sent out after observing the AR for a certain confidence interval. For example, had the concept of OHR been used to provide a warning for the X2.2 class flare for AR 12673, the exact time of sending out the alert would have been 2017 September 4 12:00 UTC (24 hr post increase in $R_{(50,15)}$) and T_{res} would have been approximately 44 hr.

5. Summary and Conclusions

Detailed information on measuring the pre-eruptive conditions in the solar atmosphere is important to obtain more accurate future solar flare-prediction methods. Korsós et al. (2020) and Korsós et al. (2022) proposed and elaborated that the prediction of major solar eruptions could be improved by incorporating data from the LSA, which extends to approximately 4 Mm above the photosphere. They noted that using PF extrapolation data allows for earlier identification of the preflare evolution phase of predictor parameters, particularly in the region above the photosphere within the LSA (up to 2 Mm). The PF offers a simplified yet insightful representation of the 3D magnetic field of an AR, capturing its essential large-scale structure without the complexities of currents. It is

important to stress here that free magnetic energy or the dynamics of flares cannot be obtained from PF extrapolation. However, PF extrapolation can provide a meaningful insight into the topology of the field, and that is where its value is in the current context (Wiegmann & Sakurai 2012; Korsós et al. 2024). Therefore, to further explore the idea of studying the pre-eruptive conditions of ARs, we made use of the concept developed by Korsós et al. (2020) and Korsós et al. (2022) and analyzed the evolution of the R -value as a function height for the selected ARs. We specifically investigated whether there is an OHR where the R -value provides certain hints about the occurrence of an upcoming large flare. Based on our case study, we conclude the following:

1. Since the R -value is a filtered version of the unsigned flux and is calculated based on the magnetic field values around high-gradient PILs, it only reinforces the argument that there may be a strong correlation between flux emergence and R -value increase.
2. The variation of R -value before the first X-class flare is quite different from that of nonflaring ARs i.e., ARs that do not host flares stronger or equal to C1.0. It is seen that the $R_{(150,15)}$ decays to zero output faster in height for nonflaring ARs compared to flaring ARs. $R_{(150,15)}$ serves as a good discriminant to distinguish between flaring and nonflaring ARs.
3. Having tested five different models of R -value with fixed values of B_{th} and D_{sep} , we found that the R -value is more sensitive to B_{th} in comparison to D_{sep} (a representative example can be found in Appendix A, for more examples see the GitHub project repository). We found that the OHR for R -value is impacted by the choice of B_{th} and there is no specific choice for B_{th} that works best for all cases. For example, considering a target height range of 0.00–3.24 Mm, a B_{th} of 100 G is a good choice to study AR 11158 but a B_{th} of 50 G works better for AR 11166 (refer to Table 5). Here, a good choice for the threshold is the one that best optimizes the response time. Overall, $R_{(50,15)}$ may be adjudged as the best performing R -value model for having maximized T_{diff} in four out of five cases. For the purpose of real-time prediction, $R_{(50,15)}$ may be primarily used for prediction, while $R_{(150,15)}$ and $R_{(100,15)}$ may be used for purposes of correlating and validating the information received slightly in advance from $R_{(50,15)}$. We have also seen that it is not necessary for an OHR to exist but provided it exists for multiple models, it is shifted to lower heights upon increasing B_{th} .
4. Previous studies on R -value have mostly focused on its evolution on the photosphere. Instead, we studied it in the LSA and we were able to define the OHR at heights where a definitive jump in the R -value was observed. Thus, the concept of OHR was extended beyond its definition based on the WG_M morphological parameter and magnetic helicity to a new parameter, such as R -value. Based on the current case study, we find that the concept of OHR when defined in terms of R -value may work best for “predicting” X-class flares which are linked to “flux emergence near PILs,” as compared to cases which do not exhibit the characteristics of flux emergence and are already associated to complex sunspots to start with (statement in general terms; statistical significance is beyond the scope of this paper). ARs 11158, 11166, 12017, and 12673 are the best examples of such cases. In

these cases, we also found that the sunspot group became progressively more complex (e.g., β -type at the start of the observation time window and $\beta\gamma\delta$ -type toward the end). However, for cases like ARs 12297 or 12158 for which an OHR could not be determined, a δ sunspot could be found throughout/or at the start of the observation time window.

5. Based on our calculations of the OHR for five ARs linked to X-class flares, we found that if the R -value is studied for a confidence interval of 24 hr, it may be possible to have an optimal time of 48–68 hr and a response time of 24–44 hr.

The biggest limitation we encountered in our study was the absence of a statistically large data set for X-class flares that satisfied the criteria discussed in Section 3. We hope that in the future, as more examples are studied, we may be able to improve the definition of a jump in R -value by reviewing the continuity interval (6 hr as defined currently). In the future, building on the approach of this study, we will also address the question of whether the joint application of different predictor parameters enhances prediction skills by applying them throughout the LSA. We plan to extend these calculations to more cases of X-class flares and weaker flares such as M-class flares and other methods of extrapolations.

Acknowledgments

This research work is supported by Space Weather Awareness Training Network (SWATNet) and it comes under the aegis of the project: “Three-Dimensional Solar Flare Forecasting” (<https://swatnet.eu/>). SWATNet has received funding from the European Union’s Horizon 2020 research and innovation program under the Marie Skłodowska-Curie Grant Agreement No. 955620. M.B.K., R.E., and M.G. acknowledge support from ISSI-BJ (“Step forward in solar flare and coronal mass ejection (CME) predicting”). RE is grateful to STFC (UK, grant No. ST/M000826/1) and PIFI (China, grant No. 2024PVA0043). M.B.K. is grateful for the Leverhulme Trust Found ECF-2023-271. M.B.K. acknowledges support by UNKP-22-4-II-ELTE-186, ELTE Hungary. R.E. and M.B.K. also thank for the support received from NKFIH OTKA (Hungary, grant No. K142987). This work was also supported by the NKFIH Excellence Grant TKP2021-NKTA-64. A.N. and S.P. acknowledge support by the ERC Synergy Grant “Whole Sun” (GAN: 810218).

Appendix A

Qualitative Comparison of Input Parameter Sensitivities: Case Study of AR 11166

Changing D_{sep} does not impact the R -value in height and time as much as changing B_{th} (see Figure 11). For a quantitative example, consider Tables 6 and 7. It may be observed from Table 6 that if B_{th} is kept fixed at 150 G, reducing D_{sep} from 15 to 10 Mm reduces the computed R -value by approximately 5%–10%, while for B_{th} fixed at 50 G, the reduction is approximately 10%–20%. However, Table 7 shows that reducing B_{th} from 150 to 100 G (with D_{sep} fixed at 15 Mm) can cause the R -value to increase by an order of magnitude (check height 1.08 Mm).

Plots for AR 11166

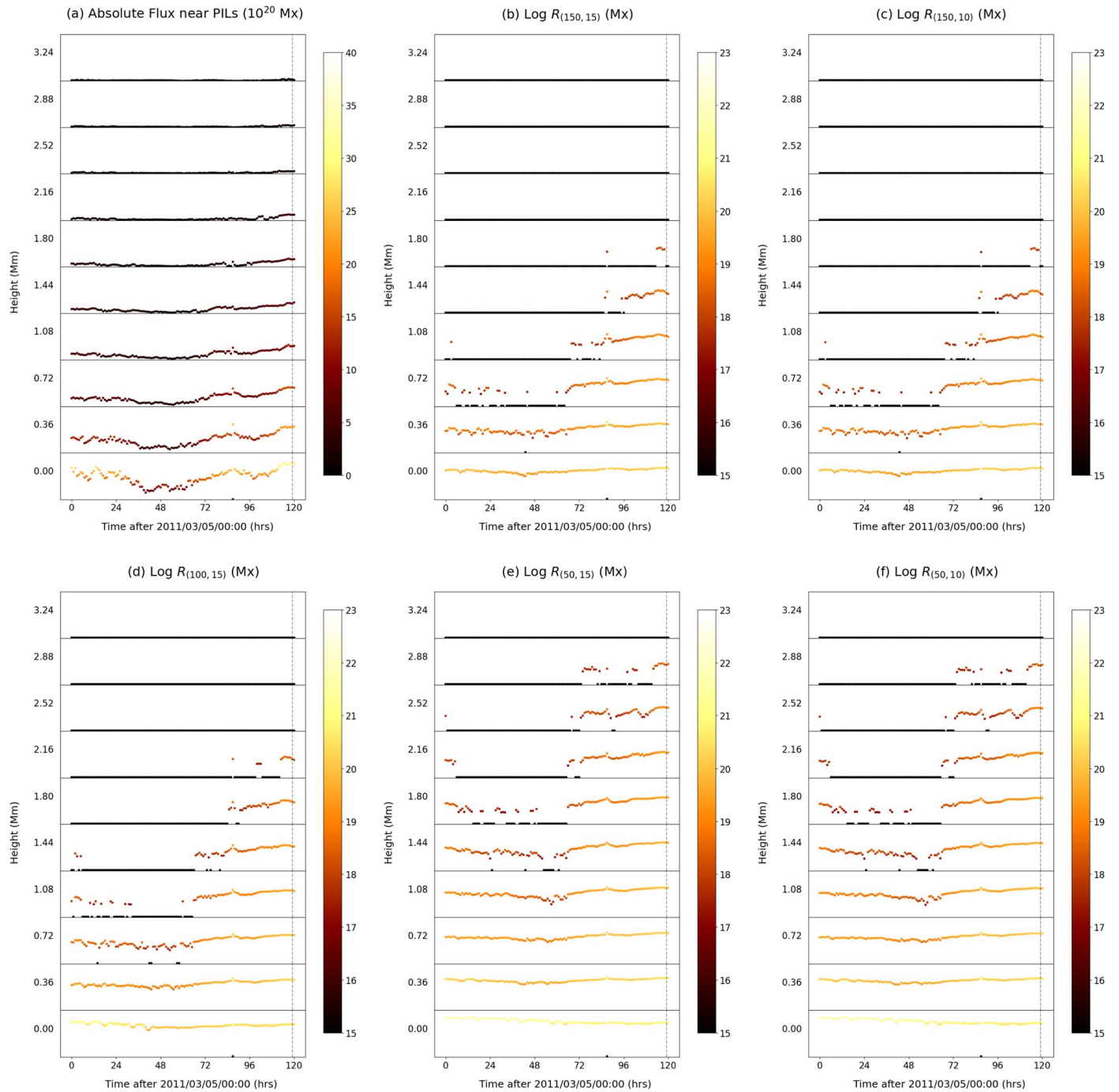


Figure 11. Multiple-height stack plots for AR 11166: (a) unsigned flux around PILs, (b) $R_{(150,15)}$, (c) $R_{(150,10)}$, (d) $R_{(100,10)}$, (e) $R_{(50,15)}$, (f) $R_{(50,10)}$; vertical dashed line indicates the time of occurrence of the X1.5 flare at 23:13 UTC on 2011 March 9; note that plots b and c do not exhibit any significant difference (same goes for plots (e) and (f)); implying that R -value is not too sensitive to D_{sep} ; the colorbar in plot a indicates unsigned flux (in 10^{20} Mx); the colorbars in plots (b)–(f) indicate the logarithm of R -value (in Mx); any black lines or points in plots (b)–(f) indicate null output.

Table 6
A Comparison of Different Models of R -values to Explore the Sensitivity to D_{sep} (Refer to Columns (5) and (8))

Unsigned Flux near PILs and R -values (both in 10^{20} Mx) for AR 11166 at 18:00 UTC, 2011 March 8							
Height (Mm) (1)	Unsigned Flux (2)	$R_{(150,15)}$ (3)	$R_{(150,10)}$ (4)	$R_{(150,10)}/R_{(150,15)}$ (5)	$R_{(50,15)}$ (6)	$R_{(50,10)}$ (7)	$R_{(50,10)}/R_{(50,15)}$ (8)
0.00	23.54	2.1758	2.0698	0.95	7.4204	6.7488	0.91
0.36	15.21	0.5619	0.5240	0.93	2.5417	2.2674	0.89
0.72	11.06	0.1382	0.1228	0.89	1.1530	0.9991	0.87
1.08	5.39	0.0114	0.0103	0.90	0.5310	0.4435	0.84
1.44	3.99	N.V.	N.V.	N.V.	0.2230	0.1812	0.81
1.80	0.90	N.V.	N.V.	N.V.	0.0626	0.0529	0.85
2.16	1.61	N.V.	N.V.	N.V.	0.0196	0.0157	0.80
2.52	0.48	N.V.	N.V.	N.V.	N.V.	N.V.	N.V.
2.88	0.18	N.V.	N.V.	N.V.	N.V.	N.V.	N.V.
3.24	0.00	N.V.	N.V.	N.V.	N.V.	N.V.	N.V.

Note. In columns (3) and (4), B_{th} is fixed at 150 G but D_{sep} is 15 and 10 Mm, respectively. In columns (6) and (7), B_{th} is fixed at 50 G but D_{sep} is 15 and 10 Mm, respectively. It is seen that $R_{(150,15)}$ is about 10% of the value of the unsigned flux near PILs on the photosphere. N.V.: No value, indicates null output.

Table 7
A Comparison of Different Models of R -value to Explore the Sensitivity to B_{th} (Refer to Columns (5), (6) and (9))

R -values (in 10^{20} Mx) for AR 11166 at 18:00 UTC, 2011 March 8								
Height (Mm) (1)	$R_{(150,15)}$ (2)	$R_{(100,15)}$ (3)	$R_{(50,15)}$ (4)	$R_{(100,15)}/R_{(150,15)}$ (5)	$R_{(50,15)}/R_{(150,15)}$ (6)	$R_{(150,10)}$ (7)	$R_{(50,10)}$ (8)	$R_{(50,10)}/R_{(150,10)}$ (9)
0.00	2.1758	3.5746	7.4204	1.64	3.41	2.0698	6.7488	3.26
0.36	0.5619	1.1095	2.5417	1.97	4.52	0.5240	2.2674	4.33
0.72	0.1382	0.3935	1.1530	2.85	8.34	0.1228	0.9991	8.13
1.08	0.0114	0.1291	0.5310	11.36	46.74	0.0103	0.4435	43.18
1.44	N.V.	0.0218	0.2230	N.V.	N.V.	N.V.	0.1812	N.V.
1.80	N.V.	N.V.	0.0626	N.V.	N.V.	N.V.	0.0529	N.V.
2.16	N.V.	N.V.	0.0196	N.V.	N.V.	N.V.	0.0157	N.V.
2.52	N.V.	N.V.	N.V.	N.V.	N.V.	N.V.	N.V.	N.V.
2.88	N.V.	N.V.	N.V.	N.V.	N.V.	N.V.	N.V.	N.V.
3.24	N.V.	N.V.	N.V.	N.V.	N.V.	N.V.	N.V.	N.V.

Note. In columns (2), (3), and (4), D_{sep} is fixed at 15 Mm but B_{th} is 150, 100, and 50 G, respectively. In columns (7) and (8), D_{sep} is fixed at 10 Mm but B_{th} is 150 and 50 G, respectively. N.V.: No value, indicates null output.

Appendix B Outlier Case of AR 11283

AR 11283 defied classification into either of the two categories as described in Section 4.1. In this AR, the two X-class flares occur between September 6 and 8, when the unsigned flux near PILs is not too high and is somewhat stable in time. However high levels of unsigned flux were reported around September 1 and after 2011 September 8. The complexity of the sunspot group gradually increased with time, β -type between September 1–5, $\beta\gamma$ -type on September 6 and $\beta\gamma\delta$ -type between September 7 and 8.

Although this AR is somewhat similar to the cases discussed in Section 4.1 (as in a significant increase in the unsigned flux is seen after September 8), it is rather distinctive when it comes to results obtained from the R -value models. At first glance, it is difficult to determine an OHR from the $R_{(150,15)}$ and $R_{(100,15)}$

models because the black lines are not continuous over a long time (48 hr) and they are not followed by a period of consistently high R -value as we have seen for cases described in 4.1 (see Figure 12). For example, $R_{(150,15)}$ at 0.72 Mm fluctuates between null and finite values before a temporary increase in R -value is seen at 22:00 UTC on September 5. However, determining an OHR for $R_{(50,15)}$ is not that difficult and the height range of 2.16–3.24 Mm is considered as the OHR. This is because a similar pattern, consistent in height, can be found for heights 2.16–2.52 Mm.

At a time of about 24 hr before the time of occurrence of the X2.1 flare, $R_{(50,15)}$ has a relatively lower value in the photosphere compared to what it is at around September 1–2. Interestingly, at the heights in the OHR, the opposite is true. $R_{(50,15)}$ sustains a finite output 24 hr before the flare but null values are seen at around September 1–2.

Plots for AR 11283

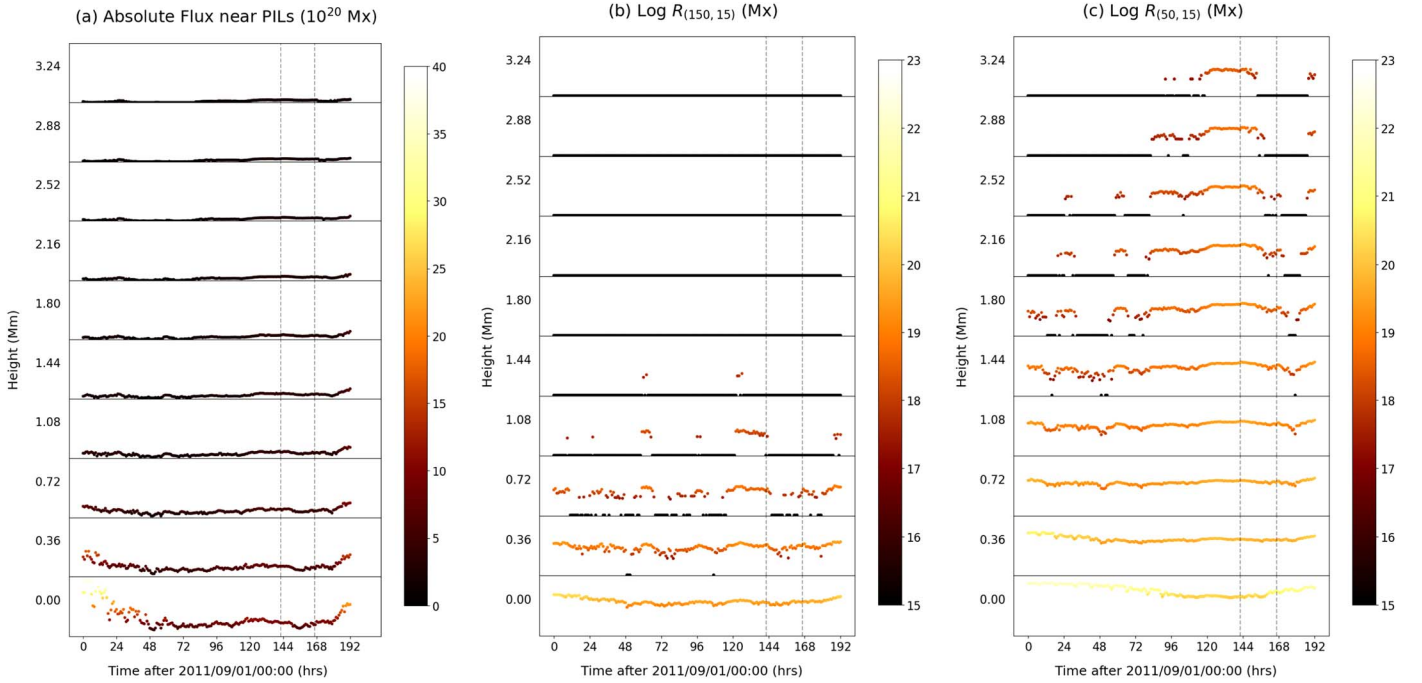


Figure 12. Multiple-height stack plots for AR 11283: (a) unsigned flux around PILs, (b) $R_{(150,15)}$, and (c) $R_{(50,15)}$; vertical dashed lines indicate X-class flare occurrence times on 2011 September 6 and 7; the colorbar in plot a indicates unsigned flux (in 10^{20} Mx); the colorbars in plots b–f indicate the logarithm of R -value (in Mx); black lines or points in plots b and c indicate null output.

Appendix C

Case Studies for Weaker Flare Classes

C.1. M-class Flares

In this section, an attempt is made to check if the preflare trends before M-class flares are similar to what we have seen previously in the case of X-class flares. This will help us understand if preflare variations of R -value (in height and time) could possibly distinguish between an impending X-class flare and an M-class flare. Since we have only studied four cases here, our motivation here is not to make explicit statistical

conclusions but to gain an insight into the R -value configuration in height and time before the first M-class flare hosted by an AR associated with a δ sunspot. The selection criteria of these cases remain the same as we had for X-class flares. The flares under focus are the first M-class flares for ARs 11620, 11719, 11818, and 12497 (refer to Table 8). We followed the same procedures as before for X-class flares to determine the OHR, T_{rv} , T_{diff} , T_{diff}^* , T_{opt} , and T_{res} for M-class flares (refer to Tables 9 and 10).

An OHR could be determined in three out of the four cases. While the evolution of R -value for ARs 11620, 11818, and 12497

Table 8

Table Listing the Details of Studied ARs, Flares, Corresponding Time Windows, and AR Dimensions

Observed Data—M-class Flares							
No.	AR	Class	T_{start}	T_{end}	$T_{flare\ onset}$	$T_{fo}-T_{start}$ (hr)	Dimensions (Mm^2)
01	11620	M2.2	2012/11/24 00:00	2012/11/30 00:00	2012/11/28 21:20	117.33	318.96×109.80
02	11719	M6.5	2013/04/08 00:00	2013/04/13 00:00	2013/04/11 06:55	78.92	388.80×247.68
03	11818	M3.3	2013/08/12 00:00	2013/08/19 00:00	2013/08/17 18:16	138.27	225.72×124.20
04	12497	M1.0	2016/02/08 00:00	2016/02/15 00:00	2016/02/12 10:36	106.60	306.00×228.60

Table 9

A List of OHRs for Different Models of R -value for M-class Flare Cases

No.	AR	OHR [$R_{(150,15)}$]	OHR [$R_{(100,15)}$]	OHR [$R_{(50,15)}$]
01	11620	0.00–1.80 Mm	0.36–2.52 Mm	0.72–3.24 Mm
02	11719	---	---	---
03	11818	0.72–1.80 Mm	1.08–2.52 Mm	1.44–3.24 Mm
04	12497	0.72–1.08 Mm	1.08–2.16 Mm	1.80–3.24 Mm

R-value plots for AR 11620

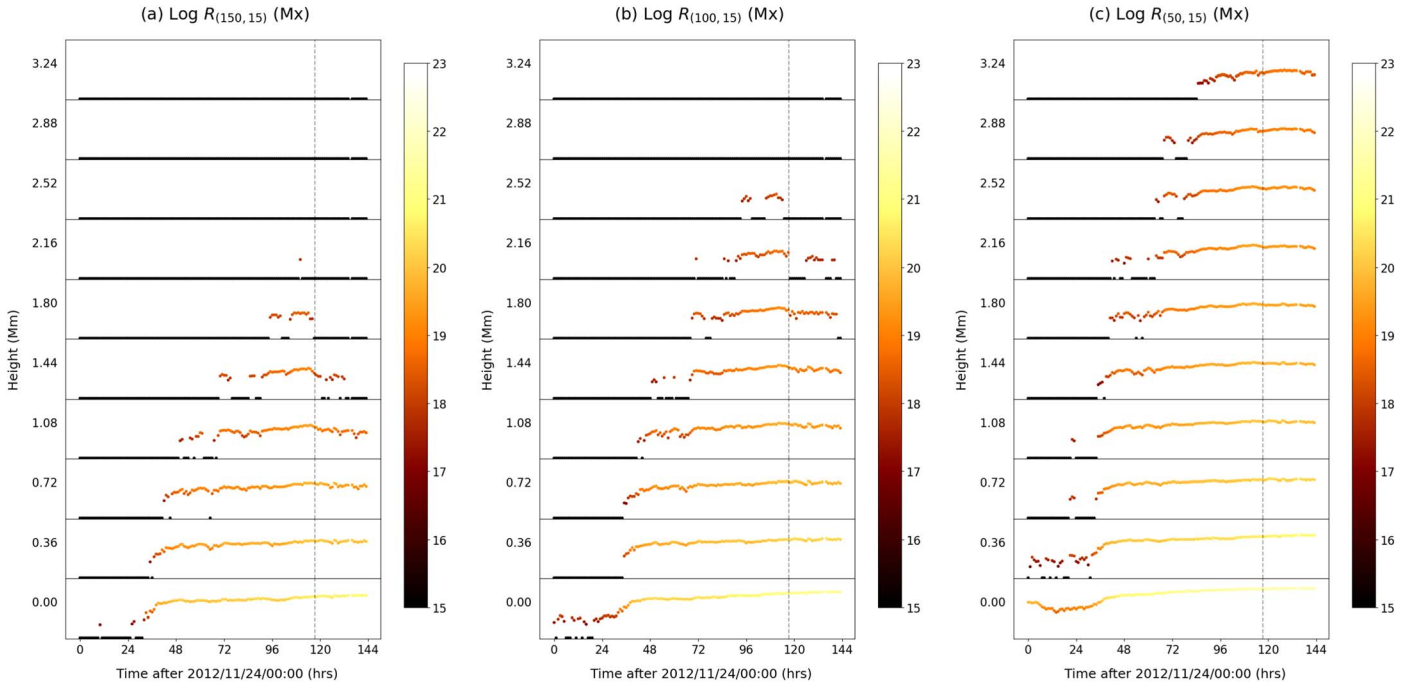


Figure 13. Multiple-height stack plots for (a) $R_{(150,15)}$, (b) $R_{(100,15)}$, and (c) $R_{(50,15)}$; vertical dashed line indicates time of occurrence of the M2.2 flare; colorbar indicates the logarithm of R -value (in Mx); any black lines or points indicate null output.

R-value plots for AR 11719

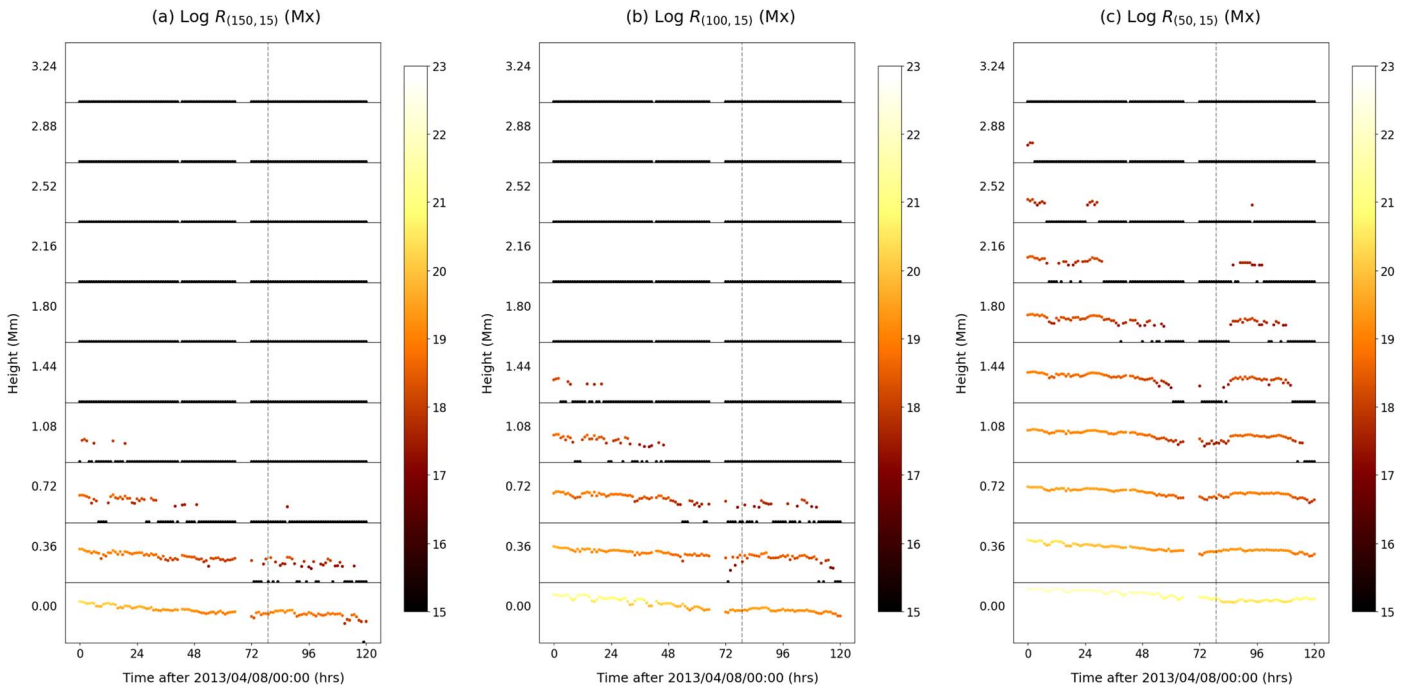


Figure 14. Multiple-height stack plots for (a) $R_{(150,15)}$, (b) $R_{(100,15)}$, and (c) $R_{(50,15)}$; vertical dashed line indicates time of occurrence of the M6.5 flare; colorbar indicates the logarithm of R -value (in Mx); any black lines or points indicate null output.

closely resembles the X-class flare cases for emerging ARs (refer to Section 4.1; e.g., see Figure 13), the evolution of R -value for AR 11719 (see Figure 14) appears similar to the cases explained in

Section 4.2. This suggests that studying the R -value along with the concept of OHR may not be sufficient in distinguishing between an impending X-class flare and an M-class flare qualitatively.

R-value plots for AR 12353

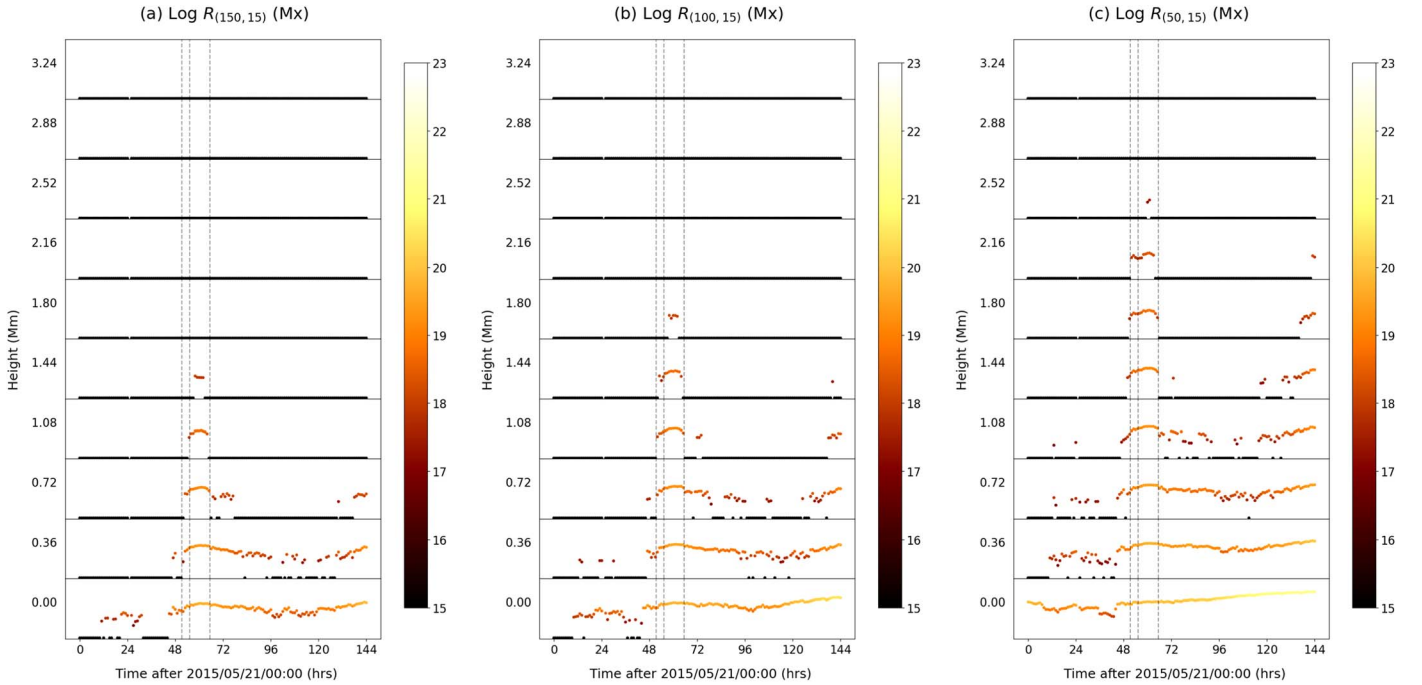


Figure 15. Multiple-height stack plots for (a) $R_{(150,15)}$, (b) $R_{(100,15)}$, and (c) $R_{(50,15)}$; vertical dashed lines indicate C-class flare occurrence times on 2015 May 23; colorbar indicates the logarithm of R -value (in Mx); any black lines or points indicate null output.

Table 10
A List of Optimal Times (Indicated in Bold) and Response Times for each OHR for X-Class Flare Cases

No. (1)	AR (2)	Flare (3)	T_{pf} (4)	T_{diff}^* [$R_{(150,15)}$] (5)	T_{diff}^* [$R_{(100,15)}$] (6)	T_{diff}^* [$R_{(50,15)}$] (7)	T_{opt} (8)	$T_{\text{res}} = T_{\text{opt}} - C_{\text{int}}$ (9)
01	11620	M2.2	2012/11/28 21:00	85 hr	82 hr	83 hr	85 hr	61 hr
02	11719	M6.5	2013/04/11 06:00	- - -	- - -	- - -	- - -	- - -
03	11818	M3.3	2013/08/17 18:00	54 hr	59 hr	97 hr	97 hr	73 hr
04	12497	M1.0	2016/02/12 10:00	18 hr	7 hr	18 hr	18 hr	-6 hr

Note. Column (4) lists the latest time-stamp preceding the flare “ T_{pf} ”; Columns (5)–(7) list the maximum lead time across all heights “ T_{diff}^* ” for $R_{(150,15)}$, $R_{(100,15)}$, and $R_{(50,15)}$, respectively. The maximum “ T_{diff}^* ” across multiple R -value models is “ T_{opt} ” and is listed in column (8); column (9) lists the response time “ T_{res} ” after subtracting the confidence interval “ C_{int} ” from T_{opt} . In the case of AR 12497, T_{opt} was less than the confidence interval “ C_{int} ” as the jump in R -value was immediately followed by an M-class flare, and hence we have a negative value for T_{res} .

C.2. C-class Flare Case: AR 12353

ARs associated with a δ sunspot are normally flaring in nature and are associated with M-class or X-class flares. It is rare for ARs hosting a δ sunspot to be solely associated with C-class flares or remain nonflaring. One such example is AR 12353, which produced three C-class flares on 2015 May 23; C1.0 (03:27 UTC); C1.1 (07:18 UTC) and C2.3 (17:30 UTC) in chronological order. In the SHARP data repository, SHARP number 5596 corresponds to not just AR 12353 but also AR 12352. Since it was not possible to isolate AR 12353, PF extrapolation and subsequent computation of $R_{(150,15)}$, $R_{(100,15)}$, and $R_{(50,15)}$ were carried out on the entire SHARP data. A jump in $R_{(150,15)}$ to nonzero values (in the photosphere) is seen at about 6 hr before the first flare. Interestingly, at heights of 0.36 and 0.72 Mm, all three C-class flares happen when $R_{(150,15)}$

shows a clear jump and is nonzero. The jump in $R_{(150,15)}$ is seen at all heights up to 1.44 Mm (see Figure 15(a)). This suggests that it could be possible that a jump in R -value may be linked to a C-class flare, hosted by an AR with a δ sunspot. The maximum value of $R_{(150,15)}$ in the photosphere observed for AR 12353 (in the time window of study) was 0.78×10^{20} Mx. It is considerably lesser (by orders) than the threshold of 20×10^{20} Mx, which when breached guarantees the occurrence of an X-class flare (Schrijver 2007).

Appendix D Additional Tables

Appendix D contains three tables (Tables 11, 12 and 13) which quantify the lead time at different heights for different R -value models.

Table 11
Lead Times T_{diff} Listed at all Heights for Different ARs (Computed using $R_{(150,15)}$)

Approximate Time Between Jump in $R_{(150,15)}$ and X-class Flare Occurrence Time, Calculated Height-wise											
No.	AR	0.00 Mm	0.36 Mm	0.72 Mm	1.08 Mm	1.44 Mm	1.80 Mm	2.16 Mm	2.52 Mm	2.88 Mm	3.24 Mm
01	11158	---	49 hr	48 hr	43 hr	33 hr	---	---	---	---	---
02	11166	---	---	54 hr	35 hr	22 hr	---	---	---	---	---
03	11283	---	---	---	20 hr	---	---	---	---	---	---
04	11520	---	---	---	---	---	---	---	---	---	---
05	12017	---	40 hr	36 hr	20 hr	---	---	---	---	---	---
06	12158	---	---	---	---	---	---	---	---	---	---
07	12297	---	---	---	---	---	---	---	---	---	---
08	12673	---	---	65 hr	57 hr	53 hr	50 hr	44 hr	40 hr	33 hr	---

Note. Text in bold indicates T_{diff}^* , i.e., the maximum lead time across all heights for a given AR).

Table 12
Lead Times T_{diff} Listed at all Heights for Different ARs (Computed using $R_{(100,15)}$)

Approximate Time Between Jump in $R_{(100,15)}$ and X-class Flare Occurrence Time, Calculated Height-wise											
No.	AR	0.00 Mm	0.36 Mm	0.72 Mm	1.08 Mm	1.44 Mm	1.80 Mm	2.16 Mm	2.52 Mm	2.88 Mm	3.24 Mm
01	11158	---	59 hr	47 hr	48 hr	43 hr	38 hr	35 hr	32 hr	---	---
02	11166	---	---	---	53 hr	52 hr	41 hr	6 hr	---	---	---
03	11283	---	---	---	---	24 hr	21 hr	---	---	---	---
04	11520	---	---	---	---	---	---	---	---	---	---
05	12017	---	---	47 hr	39 hr	20 hr	---	---	---	---	---
06	12158	---	---	---	---	---	---	---	---	---	---
07	12297	---	---	---	---	---	---	---	---	---	---
08	12673	---	---	---	65 hr	58 hr	57 hr	52 hr	50 hr	44 hr	42 hr

Note. Text in bold indicates T_{diff}^* , i.e., the maximum lead time across all heights.

Table 13
Lead Times T_{diff} Listed at all Heights for Different ARs (Computed using $R_{(50,15)}$)

Approximate Time Between Jump in $R_{(50,15)}$ and X-class Flare Occurrence Time, Calculated Height-wise											
No.	AR	0.00 Mm	0.36 Mm	0.72 Mm	1.08 Mm	1.44 Mm	1.80 Mm	2.16 Mm	2.52 Mm	2.88 Mm	3.24 Mm
01	11158	---	---	---	50 hr	48 hr	47 hr	46 hr	45 hr	43 hr	41 hr
02	11166	---	---	---	---	60 hr	53 hr	46 hr	46 hr	---	---
03	11283	---	---	---	---	---	---	61 hr	60 hr	59 hr	23 hr
04	11520	---	---	---	---	---	---	---	---	---	---
05	12017	---	---	---	48 hr	47 hr	46 hr	44 hr	---	---	---
06	12158	---	---	---	---	---	---	---	---	---	---
07	12297	---	---	---	---	---	---	---	---	---	---
08	12673	---	---	---	---	68 hr	64 hr	61 hr	60 hr	57 hr	54 hr

Note. Text in bold indicates T_{diff}^* , i.e., the maximum lead time across all heights.

ORCID iDs

Shreyesh Biswal  <https://orcid.org/0000-0002-1367-8326>
 Marianna B. Korsós  <https://orcid.org/0000-0002-0049-4798>
 Manolis K. Georgoulis  <https://orcid.org/0000-0001-6913-1330>
 Alexander Nindos  <https://orcid.org/0000-0003-0475-2886>
 Spiros Patsourakos  <https://orcid.org/0000-0003-3345-9697>
 Robertus Erdélyi  <https://orcid.org/0000-0003-3439-4127>

References

- Alissandrakis, C. E. 1981, *A&A*, **100**, 197
 Archontis, V., Moreno-Insertis, F., Galsgaard, K., Hood, A., & O'Shea, E. 2004, *A&A*, **426**, 1047
 Aulanier, G., Janvier, M., & Schmieder, B. 2012, *A&A*, **543**, A110
 Aulanier, G., Török, T., Démoulin, P., & DeLuca, E. E. 2010, *ApJ*, **708**, 314
 Bobra, M. G., Sun, X., Hoeksema, J. T., et al. 2014, *SoPh*, **289**, 3549
 Burtseva, O., & Petrie, G. 2013, *SoPh*, **283**, 429
 Campi, C., Benvenuto, F., Massone, A. M., et al. 2019, *ApJ*, **883**, 150
 Carmichael, H. 1964, *NASSP*, **50**, 451
 Dere, K. P., Brueckner, G. E., Howard, R. A., Michels, D. J., & Delaboudiniere, J. P. 1999, *ApJ*, **516**, 465
 Erdélyi, K., Marianna, B., Huang, X., et al. 2022, *JSWSC*, **12**, 2
 Falconer, D. A., Moore, R. L., & Gary, G. A. 2002, *ApJ*, **569**, 1016
 Falconer, D. A., Moore, R. L., & Gary, G. A. 2003, *JGRA*, **108**, 1380
 Fan, Y. 2001, *ApJ*, **554**, L111
 Gary, G. A. 1989, *ApJS*, **69**, 323
 Georgoulis, B., Shaun, D., Michele, P., et al. 2021, *JSWSC*, **11**, 39
 Georgoulis, M. K., Nindos, A., & Zhang, H. 2019, *RSPTA*, **377**, 20180094
 Georgoulis, M. K., & Rust, D. M. 2007, *ApJ*, **661**, L109
 Georgoulis, M. K., Titov, V. S., & Mikić, Z. 2012, *ApJ*, **761**, 61
 Gopalswamy, N. 2016, *GSL*, **3**, 8
 Gosling, J. T. 1990, *Physics of magnetic flux ropes* (Washington, DC: AGU), 343

- Harrison, R. A. 1995, *A&A*, **304**, 585
- Hirayama, T. 1974, *SoPh*, **34**, 323
- Janvier, M. 2017, *JPIPh*, **83**, 535830101
- Janvier, M., Aulanier, G., Pariat, E., & Démoulin, P. 2013, *A&A*, **555**, A77
- Kaisig, M., Tajima, T., Shibata, K., Nozawa, S., & Matsumoto, R. 1990, *ApJ*, **358**, 698
- Kliem, B., Su, Y. N., van Ballegoijen, A. A., & DeLuca, E. E. 2013, *ApJ*, **779**, 129
- Kontogiannis, I., Georgoulis, M. K., Park, S.-H., & Guerra, J. A. 2017, *SoPh*, **292**, 159
- Kopp, R. A., & Pneuman, G. W. 1976, *SoPh*, **50**, 85
- Korsós, M. B., Baranyi, T., & Ludmány, A. 2014, *ApJ*, **789**, 107
- Korsós, M. B., Chatterjee, P., & Erdélyi, R. 2018, *ApJ*, **857**, 103
- Korsós, M. B., Erdélyi, R., Huang, X., & Morgan, H. 2022, *ApJ*, **933**, 66
- Korsós, M. B., Georgoulis, M. K., Gyenge, N., et al. 2020, *ApJ*, **896**, 119
- Korsós, M. B., Gyenge, N., Baranyi, T., & Ludmány, A. 2015, *JApA*, **36**, 111
- Korsós, M. B., Jarolim, R., Erdélyi, R., et al. 2024, *ApJ*, **962**, 171
- Künzel, H. 1959, *AN*, **285**, 271
- Kusano, K., Bamba, Y., Yamamoto, T. T., et al. 2012, *ApJ*, **760**, 31
- Kusano, K., Iju, T., Bamba, Y., & Inoue, S. 2020, *Sci*, **369**, 587
- Liu, L., Cheng, X., Wang, Y., & Zhou, Z. 2019, *ApJ*, **884**, 45
- Liu, Y., Hoeksema, J. T., Scherrer, P. H., et al. 2012, *SoPh*, **279**, 295
- Low, B. C. 1994, in Proc. of the Third SOHO Workshop, 373, Solar Dynamic Phenomena and Solar Wind Consequences, ed. J. J. Hunt (Paris: European Space Agency), 123
- Mason, J., & Hoeksema, T. 2010, *ApJ*, **723**, 634
- Parker, E. N. 1955, *ApJ*, **121**, 491
- Parker, E. N. 1979, *ApJ*, **230**, 905
- Pesnell, W. D., Thompson, B. J., & Chamberlin, P. C. 2012, *SoPh*, **275**, 3
- Pontin, D. I., & Priest, E. R. 2022, *LRSP*, **19**, 1
- Sammis, I., Tang, F., & Zirin, H. 2000, *ApJ*, **540**, 583
- Scherrer, P. H., Schou, J., Bush, R. I., et al. 2012, *SoPh*, **275**, 207
- Schrijver, C. J. 2007, *ApJL*, **655**, L117
- Shibata, K., Nozawa, S., Matsumoto, R., Sterling, A. C., & Tajima, T. 1990, *ApJL*, **351**, L25
- Shibata, K., Tajima, T., Steinolfson, R. S., & Matsumoto, R. 1989, *ApJ*, **345**, 584
- Sturrock, P. A. 1966, *Natur*, **211**, 695
- Temmer, M., Veronig, A. M., Kontar, E. P., Krucker, S., & Vršnak, B. 2010, *ApJ*, **712**, 1410
- Tian, L., Liu, Y., & Wang, J. 2002, *SoPh*, **209**, 361
- Toriumi, S. 2022, *AdSpR*, **70**, 1549
- Toriumi, S., & Wang, H. 2019, *LRSP*, **16**, 3
- Wiegelmann, T., & Sakurai, T. 2012, *LRSP*, **9**, 5
- Yashiro, S., Gopalswamy, N., Akiyama, S., Michalek, G., & Howard, R. A. 2005, *JGRA*, **110**, A12S05
- Youssef, M. 2012, *JAsGe*, **1**, 172
- Zhang, J., Dere, K. P., Howard, R. A., & Vourlidas, A. 2004, *ApJ*, **604**, 420
- Zhang, J., Wang, J., Deng, Y., & Wu, D. 2001, *ApJ*, **548**, L99